

# Technical Memorandum



**Date:** October 12, 2016  
**To:** PFC 5 Documentation Set  
**From:** David Potyondy  
**Re:** Hill Contact Model [version 4]  
**Ref:** ICG7795-L

This memo describes the hill contact model (version 4) as provided in the material-modeling support package for PFC 5.0.<sup>1</sup> A hill material is defined as a granular assembly in which the hill contact model exists at all grain-grain contacts, and this material behaves like an unsaturated granular material. The model formulation and test problems are provided in the first and second major sections, respectively. The test problems consist of a two-grain system, a grain assembly and a material-behavior study. The material-behavior study creates hill and linear materials to represent a typical aggregate base layer of an asphalt-surface roadway, and subjects them to triaxial testing to discern the effect of material type on material behavior. The creation and triaxial testing of a hill material is described in Potyondy (2016, User-Defined Material Example). A pavement-design package that supports creation and triaxial testing of the hill material containing geogrid is described in Potyondy et al. (2016).

---

<sup>1</sup> The material-modeling support package is described in Potyondy (2016). The hill contact model is referred to in commands and FISH by the name **hill**, and is provided as a dynamic link library (DLL) file that is loaded into *PFC3D* at runtime. The version number of the hill contact model is given by the command **{list contact modellist}** and listed in the “Minor” column.

## TABLE OF CONTENTS

1.0 FORMULATION .....	3
1.1 Notational Conventions .....	3
1.2 The PFC Model .....	3
1.3 Kinematic Variables .....	5
1.4 Hill Material .....	8
1.5 Activity-Deletion Criteria .....	12
1.6 Force-Displacement Law .....	12
1.7 Properties .....	16
1.8 Methods .....	18
1.9 Time Step Estimation Scheme .....	19
2.0 TEST PROBLEMS .....	20
2.1 Two Granite Grains .....	20
2.2 Assembly of Granite Grains .....	31
2.3 Material-Behavior Study .....	32
3.0 REFERENCES .....	38
APPENDIX A: INCREMENTAL UPDATE OF SHEAR FORCE .....	40

## 1.0 FORMULATION

The formulation of the hill contact model is provided in this section. The first three subsections summarize the notational conventions, the PFC model and the kinematic variables — refer to Itasca (2016, PFC Model Components) and Potyondy (2015) for a complete description of these concepts. The remaining subsections contain the formulation which begins with a definition of the hill material and is followed by the activity-deletion criteria, force-displacement law, properties, methods and time step estimation scheme of the hill contact model.

### 1.1 Notational Conventions

Vectors are denoted by boldface type, such as  $\mathbf{v}$ . The length or magnitude of  $\mathbf{v}$  is denoted  $\|\mathbf{v}\|$  or simply  $v$ . The addition of a hat denotes a unit vector, such that  $\hat{\mathbf{v}} = \mathbf{v}/\|\mathbf{v}\|$ . The addition of a dot denotes a time derivative, such as  $\dot{\mathbf{v}} = \partial\mathbf{v}/\partial t$ . There is a global coordinate system ( $xyz$ ). The vector  $\mathbf{v}$  can be expressed in the global coordinate system by the relations:

$$\begin{aligned} \mathbf{v} &= \mathbf{v}(x, y, z) = v_x \hat{\mathbf{i}} + v_y \hat{\mathbf{j}} + v_z \hat{\mathbf{k}} \\ \text{with } v_x &= \mathbf{v} \cdot \hat{\mathbf{i}}, \quad v_y = \mathbf{v} \cdot \hat{\mathbf{j}}, \quad v_z = \mathbf{v} \cdot \hat{\mathbf{k}} \end{aligned} \tag{1}$$

where  $\hat{\mathbf{i}}$ ,  $\hat{\mathbf{j}}$  and  $\hat{\mathbf{k}}$  are unit vectors directed along the positive  $x$ ,  $y$  and  $z$  axes, respectively.

### 1.2 The PFC Model

The PFC programs (*PFC2D* and *PFC3D*) provide a general purpose, distinct-element modeling framework that includes a computational engine and a graphical user interface. A particular instance of the distinct-element model is referred to as a *PFC model*, which refers to both the 2D and 3D models. The PFC model simulates the movement and interaction of many finite-sized particles. The particles are rigid bodies with finite mass that move independently of one another and can both translate and rotate. Particles interact at pair-wise contacts by means of an internal force and moment. Contact mechanics is embodied in particle-interaction laws that update the internal forces and moments. The time evolution of this system is computed via the distinct-element method, which provides an explicit dynamic solution to Newton's laws of motion. The PFC model provides a synthetic material consisting of an assembly of rigid grains that interact at contacts and includes both granular and bonded materials.

We here generalize and expand upon the definition of the PFC model given above. The PFC model simulates the movement of particles and their mechanical interaction at pair-wise contacts. We denote each particle as a *body* to clarify that it is not a point mass, but instead, is a rigid body with finite mass and a well-defined surface. The PFC model consists of bodies and *contacts* (see Figure 1). There are three types of bodies: *spheres*, *clumps* and *walls*. Bodies have surface properties that are

assigned to the *pieces* on the body surface. A ball consists of one piece, which is the ball itself, while the pieces of a clump and wall are called *pebbles* and *facets*, respectively. A ball is a rigid unit-thickness disk in 2D or sphere in 3D. A clump is a collection of pebbles that are rigid unit-thickness disks in 2D or spheres in 3D. Clumps model arbitrarily shaped rigid bodies. The pebbles comprising a clump can overlap but contacts do not exist between them; instead, contacts form between the pebbles on the boundary of a clump and other bodies. A wall is a collection of facets that are linear segments in 2D or triangles in 3D and that form a manifold and orientable surface.

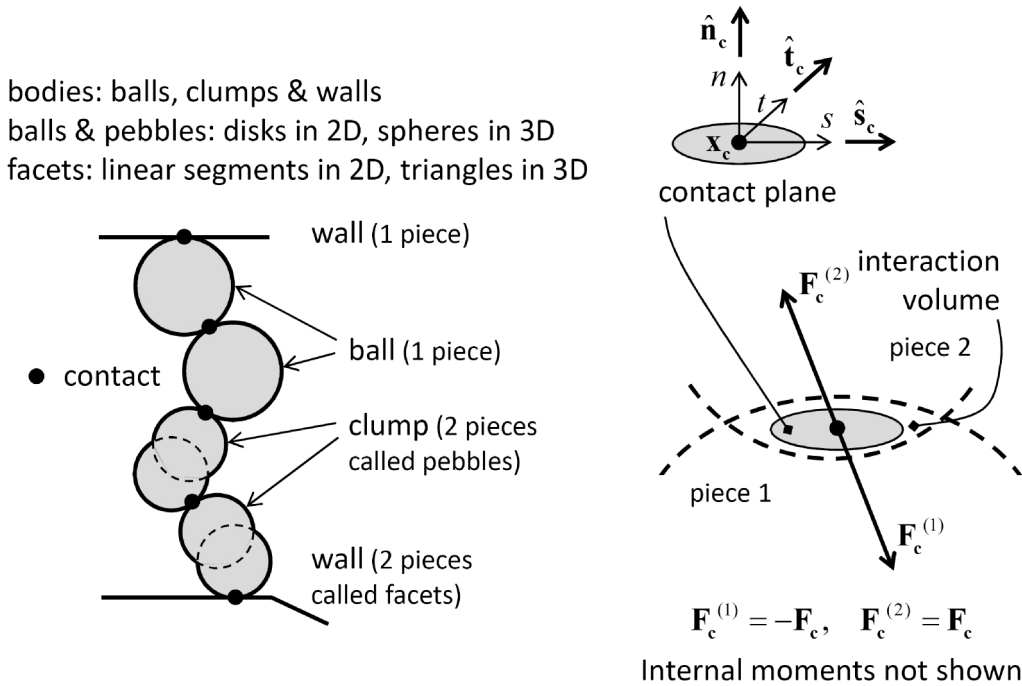


**Figure 1** PFC model showing bodies and contacts (left) and contact plane with internal force (right). (From Fig. 1 of Itasca [2016]<sup>2</sup>.)

Contact mechanics is embodied in particle-interaction laws that employ a soft-contact approach for which all deformation occurs at the contacts between the rigid bodies. The mechanical interaction between the surfaces of two bodies occurs at one or more pair-wise mechanical contacts. Contacts are created and deleted based on body proximity by the contact-detection logic. A contact provides an interface between two pieces. The interface consists of a contact plane with location ( $x_c$ ), normal direction ( $\hat{n}_c$ ) and coordinate system ( $nst$ ). The contact plane is centered within the interaction volume (either gap or overlap) of the two pieces, oriented tangential to the two pieces and rotated to ensure that relative motion of the piece surfaces remains symmetric w.r.t. the contact plane. Each contact stores a force ( $F_c$ ) and moment ( $M_c$ ) that act at the contact location in an equal

<sup>2</sup> In documentation set at PFC Model Components: PFC Model Formulation: Model Components.

and opposite sense on the two pieces. The internal force and moment are updated by the particle-interaction law, which takes the relative motion and surface properties of the two pieces as input. We refer to the particle-interaction law as a *contact model*.

### 1.3 Kinematic Variables

Kinematics considers the motion of systems of bodies without regard to the role of the forces causing the motion, while kinetics considers the relationship of the forces to the kinematic variables. The kinetics of the PFC model is embodied in the force-displacement law of each contact model. The kinematic variables that serve as the input to the force-displacement law are discussed here.

Contact resolution occurs when a new contact is detected during the cycle sequence, prior to the force-displacement calculations. During contact resolution, the contact state variables (see Table 1) are updated. Each contact model uses its properties along with the relative motion of the two contacting pieces to update the contact force and moment.

**Table 1 Contact State Variables**

Property	Description
$m_c$	effective inertial mass
<b>Contact plane</b> (see Figures 1 and 2):	
$\mathbf{x}_c$	contact-plane location
$\hat{\mathbf{n}}_c$	contact-plane normal direction
$\hat{\mathbf{s}}_c$	contact-plane coord. system ( $s$ axis)
$\hat{\mathbf{t}}_c$	contact-plane coord. system ( $t$ axis)
$g$	contact gap ( $g_c > 0$ is open)
<hr/>	
<b>Relative motion</b> (see Figure 3):	
$\dot{\delta}$	relative translational velocity
$\dot{\theta}$	relative rotational velocity
$\Delta\delta_n$	relative normal-displacement increment ( $\Delta\delta_n > 0$ is opening)
$\Delta\delta_s$	relative shear-displacement increment
$\Delta\theta_t$	relative twist-rotation increment

$\Delta\theta_b$	relative bend-rotation increment $(\Delta\theta_{bs}, \Delta\theta_{bt})$
------------------	---

The contact shown in Figure 2 has been created between the pieces of two bodies. Each contact has two ends, **end1** and **end2**, with the associated pieces and bodies labelled 1 and 2. The bodies are rigid; therefore, the motion of body  $(b)$  is described by its rotational velocity  $(\omega^{(b)})$  and the translational velocity  $(\dot{\mathbf{x}}^{(b)})$  of its centroid  $(\mathbf{x}^{(b)})$ . The contact state variables include the contact-plane information as well as the contact gap  $(g_c)$ , which is the minimal signed distance separating the piece surfaces. A vector quantity that lies on the contact plane ( $\mathbf{S}$ ) can be expressed in the contact plane coordinate system by the relations:

$$\begin{aligned}\mathbf{S} = \mathbf{S}(s, t) &= S_s \hat{\mathbf{s}}_c + S_t \hat{\mathbf{t}}_c \\ \text{with } S_s &= \mathbf{S} \cdot \hat{\mathbf{s}}_c, \quad S_t = \mathbf{S} \cdot \hat{\mathbf{t}}_c.\end{aligned}\tag{2}$$

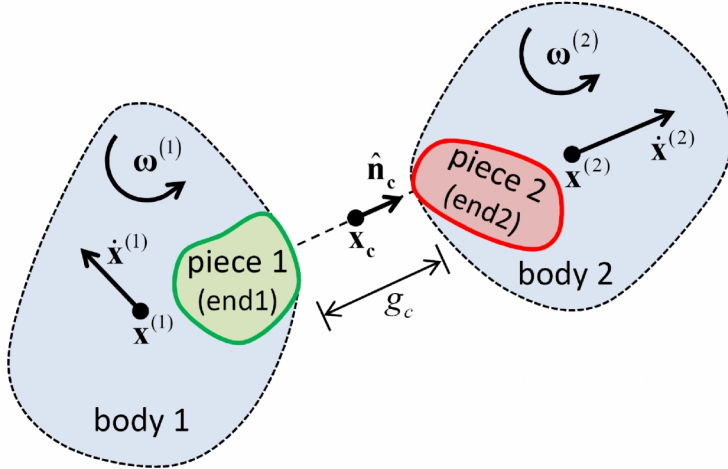


**Figure 2 A contact between the pieces of two bodies.** (From Fig. 1 of Itasca [2016]<sup>3</sup>.)

The relative motion of the piece surfaces at a contact is described by the relative translational  $(\dot{\delta})$  and rotational  $(\dot{\theta})$  velocities<sup>4</sup>:

$$\begin{aligned}\dot{\delta} &= \dot{\mathbf{x}}_c^{(2)} - \dot{\mathbf{x}}_c^{(1)} \\ \dot{\theta} &= \omega^{(2)} - \omega^{(1)}.\end{aligned}\tag{3}$$

<sup>3</sup> In documentation set at PFC Model Components: Contacts and Contact Models: Contact Resolution.

<sup>4</sup> The relative rotational velocity is not employed by the hill contact model; thus, it is omitted from the following summary.

In this expression,  $\dot{\mathbf{x}}_c^{(b)}$  is the translational velocity of body  $(b)$  at the contact location:

$$\dot{\mathbf{x}}_c^{(b)} = \dot{\mathbf{x}}^{(b)} + \boldsymbol{\omega}^{(b)} \times (\mathbf{x}_c - \mathbf{x}^{(b)}) \quad (4)$$

where  $\dot{\mathbf{x}}^{(b)}$  is the translational velocity of body  $(b)$ ;  $\boldsymbol{\omega}^{(b)}$  is the rotational velocity of body  $(b)$ ;  $\mathbf{x}_c$  is the contact location and  $\mathbf{x}^{(b)}$  is either the centroid (if the body is a ball or clump) or the center of rotation (if the body is a wall) of body  $(b)$ . The contact location defines a point that is fixed w.r.t. each body, and thus,  $\dot{\mathbf{x}}_c^{(b)}$  is the translational velocity of that point in body  $(b)$ .<sup>5</sup>

The relative translational velocity can be expressed as

$$\begin{aligned} \dot{\boldsymbol{\delta}} &= \dot{\boldsymbol{\delta}}_n + \dot{\boldsymbol{\delta}}_s \\ \text{with } \dot{\boldsymbol{\delta}}_n &= (\dot{\boldsymbol{\delta}} \cdot \hat{\mathbf{n}}_c) \hat{\mathbf{n}}_c = \dot{\delta}_n \hat{\mathbf{n}}_c, \quad \dot{\boldsymbol{\delta}}_s = \dot{\boldsymbol{\delta}} - \dot{\boldsymbol{\delta}}_n \end{aligned} \quad (5)$$

where  $\dot{\boldsymbol{\delta}}_n$  ( $\dot{\delta}_n > 0$  is moving apart) and  $\dot{\boldsymbol{\delta}}_s$  are the relative translational velocities normal and tangential, respectively, to the contact plane, and the subscripts  $n$  and  $s$  correspond with normal and shear action, respectively (see Figure 3 — the centering of the contact within the interaction volume ensures that the relative displacement is symmetric w.r.t. the contact plane).

The relative displacement increment at the contact during a time step  $\Delta t$  is

$$\begin{aligned} \Delta \boldsymbol{\delta} &= \Delta \delta_n \hat{\mathbf{n}}_c + \Delta \boldsymbol{\delta}_s \left[ \Delta \delta_{ss} = \Delta \boldsymbol{\delta}_s \cdot \hat{\mathbf{s}}_c, \quad \Delta \delta_{st} = \Delta \boldsymbol{\delta}_s \cdot \hat{\mathbf{t}}_c \right] \\ \text{with } \Delta \delta_n &= \dot{\delta}_n \Delta t, \quad \Delta \boldsymbol{\delta}_s = \dot{\boldsymbol{\delta}}_s \Delta t \end{aligned} \quad (6)$$

where  $\Delta \delta_n$  is the relative normal-displacement increment and  $\Delta \boldsymbol{\delta}_s$  is the relative shear-displacement increment.

---

<sup>5</sup> The location of this point within each body may change — e.g., under increasing applied compression, the overlap increases and these points move deeper into each body.

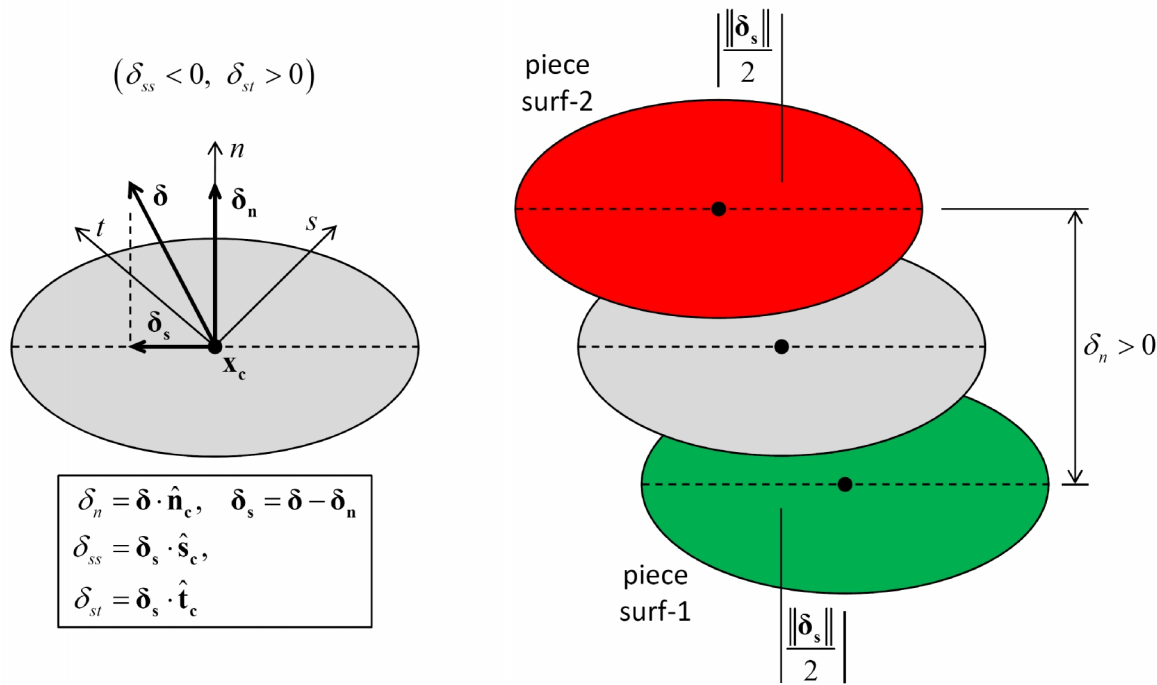


**Figure 3** *Kinematics of a contact showing contact plane with relative displacement and motion of piece surfaces.* (From Fig. 7 of Itasca [2016]<sup>6</sup>.)

#### 1.4 Hill Material

The present implementation of the hill contact model follows that of Tan and co-workers (Tan et al., 2014b), who refer to the synthetic material as a computational framework that “... has the potential to model a wide range of granular bases explicitly taking into account the coarse particle size distribution as well as the effects of moisture and fine particles.<sup>7</sup> The coarse particle size distribution is represented explicitly through the [discrete element] DEM particles. The fine particle size distribution and moisture are represented implicitly via the force model between the coarser DEM particles.” Tan and co-workers suggest that this DEM approach “... offers a viable alternative to continuum models in which the form of the bulk moduli must be empirically determined. In contrast, the calibrated DEM model represents coarse particle movement distinctly and captures ... complex trends associated with particle size distribution and moisture content measured in experiments.”

A hill material is defined as a granular assembly in which the hill contact model exists at all grain-grain contacts, and this material behaves like an unsaturated granular material. A hill material is

<sup>6</sup> In documentation set at PFC Model Components: Contacts and Contact Models: Contact Resolution.

<sup>7</sup> The hill contact model is described in Tan et al. (2014b), and is also described as Moisture Model III in Tan et al. (2014a). The present implementation follows Tan et al. (2014b), but differs by providing an incremental (as opposed to an absolute) update of the shear force that is more appropriate for static grain assemblies (see Appendix A).

defined by the following parameters (see Table 2): local radii of grains ( $R_p$ ), Young's moduli, Poisson's ratios and densities of grains ( $\{E_g, \nu_g, \rho_g\}$ ), friction coefficient ( $\mu$ ), damping constant ( $\alpha_h$ ), suction ( $\psi$ ) and moisture gap ( $g_m$ ).<sup>8</sup> These parameters are used to set the grain mass and properties of the hill contact model (listed in Section 1.7).

**Table 2 Hill Material Parameters**

Parameter	Type	Range	Default	Description
Material microproperties are listed via <code>@mpListMicroProps</code> .				
Common material parameters are listed in Table 1 of Potyondy (2016).				
Packing parameters are listed in Table 7 of Potyondy (2016).				
Add moisture via <code>@hlm_makeWet(<math>\psi</math>, <math>g_m</math>)</code> , where $\psi$ is suction and $g_m$ is moisture gap. Remove moisture via <code>@hlm_makeDry</code> .				
Set and modify the following properties via <code>@hlm_setMatBehavior</code> .				
<b>Hill material group:</b>				
$E_g$ , <code>hlm_youngMod</code>	FLT	$[0.0, \infty)$	0.0	Young's modulus of grains
$\nu_g$ , <code>hlm_poisRatio</code>	FLT	$(-1.0, 0.5]$	0.0	Poisson's ratio of grains
$\mu$ , <code>hlm_fricCoef</code>	FLT	$[0.0, \infty)$	0.0	friction coefficient
$\alpha_h$ , <code>hlm_dampCon</code>	FLT	$[0.0, 1.0]$	0.0	damping constant
$\psi$ , <code>hlm_suction</code>	FLT	$[0.0, \infty)$	0.0	suction

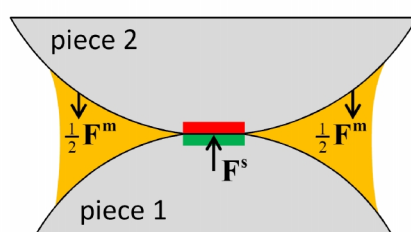
The hill contact model may exist only at a grain-grain contact. The grain-grain system behaves like two locally elastic spheres that may have a liquid bridge (see Figure 4). The liquid bridge is present if the moisture state is wet, and absent if the moisture state is dry. The hill contact model provides the behavior of an infinitesimal, nonlinear elastic (no tension) and frictional interface that carries a compressive surface-interaction force and may carry a tensile moisture force. The contact force ( $\mathbf{F}_c$ ) is the sum of the surface-interaction and moisture force, and the contact moment is zero.

<sup>8</sup> The grain shape, size distribution and density ( $\rho_g$ ) are listed in Table 1 of Potyondy (2016). If grains are clumps, then the local radii are the piece radii. Grain density is used to obtain grain mass ( $m_g$ ). If quasi-static conditions are enforced via local damping, then the damping constant is set to zero, and the local-damping factor ( $\alpha$ ) is set to 0.7.

Surface-interaction force ( $\mathbf{F}^s = \mathbf{F}^h + \mathbf{F}^d$ ). Moisture force ( $\mathbf{F}^m$ ).

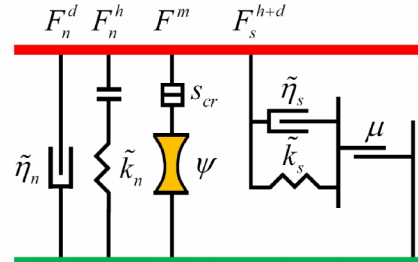
Hertz-Mindlin force ( $\mathbf{F}^h$ ), nonlinear elastic (no tension) and frictional.

Dashpot force ( $\mathbf{F}^d$ ), viscous.



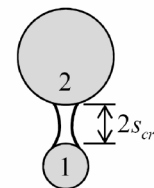
$$\mathbf{F}_c = \mathbf{F}^s + \mathbf{F}^m = \mathbf{F}^h + \mathbf{F}^d + \mathbf{F}^m$$

$$\mathbf{M}_c \equiv \mathbf{0}$$



$$\{\tilde{k}_n, \tilde{k}_s, \tilde{\eta}_n, \tilde{\eta}_s\} = f(R_p, E_b, \nu_b, m_b, \alpha_h)$$

$$\text{hill material params. } \{R_p, E_g, \nu_g, m_g, \mu, \alpha_h, \psi, g_m\}$$



$$s_{cr} = \min(R_1, R_2)$$

Liquid bridge ruptures making  $F^m = 0$ , when contact gap is greater than  $2s_{cr}$ .

**Figure 4 Behavior and rheological components of the wet hill contact model. The forces acting on piece 2 are shown, equal and opposite forces act on piece 1.**

The surface-interaction force model is based on Hertz-Mindlin contact theory along with a damping mechanism and Coulomb sliding friction (Tsuji et al., 1992). The surface-interaction force consists of Hertzian and dashpot components ( $\mathbf{F}^s = \mathbf{F}^h + \mathbf{F}^d$ ) with the Hertz-Mindlin springs acting in parallel with the dashpots. The Hertz-Mindlin springs provide the nonlinear force-displacement response arising from the mutual compression of two elastic bodies, which induces a local deformation of the bodies in the vicinity of the contact surface.<sup>9</sup> The local deformation is determined by the shapes and elastic constants of the bodies in the vicinity of the contact surface.<sup>10</sup> Slip is accommodated by imposing a Coulomb limit on the total shear force ( $F_s \leq \mu F_n$ ) via the friction coefficient ( $\mu$ ). The stiffness and damping coefficients ( $\{\tilde{k}_n, \tilde{k}_s, \tilde{\eta}_n, \tilde{\eta}_s\}$ ) are internal model parameters that are obtained

<sup>9</sup> The nonlinear contact formulation of the Hertz-Mindlin springs is an approximation of the Hertz-Mindlin contact theory of Mindlin and Deresiewicz (1953), for which the normal force-displacement response is nonlinear elastic, and the tangential force-displacement response is nonlinear inelastic caused by the growth of a slip annulus emanating from the periphery of the contact surface. The inelastic behavior means that not only do the changes in stresses and displacement depend upon the initial state of loading, but also upon the entire past history of loading and instantaneous relative rates of change of the normal and tangential forces. The inelastic tangential behavior is removed in the formulation of the Hertz-Mindlin springs by using a tangential stiffness equal to the initial tangential stiffness before tangential motion occurs. The initial tangential stiffness depends on the normal force, and corresponds with the simplest case of varying oblique forces: application of normal force, followed by tangential force increasing monotonically from zero. The normal force-displacement response is obtained from Timoshenko and Goodier (1970, p. 409), and the tangential force-displacement response for the general case of different sphere radii and different elastic constants is obtained from the initial tangential compliance in Mindlin (1949, Eq. 78).

<sup>10</sup> The formulation of the Hertz-Mindlin springs is applicable to sphere-sphere and sphere-plane contacts between two linear elastic isotropic bodies. For the sphere-plane case, the radius of the body with the planar surface can be set to infinity. The present implementation of the hill contact model does not support sphere-plane contacts.

from the radii of the contacting pieces ( $R_p$ ), the Young's moduli, Poisson's ratios and masses of the contacting bodies ( $\{E_b, \nu_b, m_b\}$ ), and the damping constant ( $\alpha_h$ ).<sup>11</sup>

The moisture-force model is inspired by liquid-bridge models, which mechanistically capture the effect of liquid dispersed among particles on the macroscopic response of the granular system (Lian et al., 1993; Muguruma et al., 2000; Richefeu et al., 2008). The moisture force ( $\mathbf{F}^m$ ) is present only if the moisture state is wet. It is an attractive force in the normal direction that is maximum when the pieces are in contact and decays exponentially until the contact gap reaches a critical value ( $2s_\sigma$ ) at which the liquid bridge ruptures, making the moisture state dry and the force zero (see Figure 6). The moisture effect is accounted for in the hill material by considering the suction (negative pore pressure) associated with surface tension that holds pore water at the interparticle contacts in unsaturated granular material. The suction can be estimated from empirical relationships that relate suction of an unsaturated granular mixture to its volumetric moisture content, mixture composition, and bulk density (Gupta and Larson, 1979; Gupta et al., 2005&2007). These relationships are embodied in a suction parameter ( $\psi$  that is given as  $\tau_{DEM_{eq}}$  in Table 3 of Tan et al. (2014b)).<sup>12</sup> Moisture is modeled in the hill material by adding suction between selected grains using the following procedure. Each hill contact has a moisture state that can be either wet or dry. When new grain-grain contacts form, they are assigned the dry hill contact model. Moisture can be added to the hill material at any time during a simulation via `@h1m_makeWet( $\psi$ ,  $g_m$ )`, where  $\psi$  is the suction

<sup>11</sup> The damping constant is related directly to the coefficient of restitution in Fig. 4 of Tsuji et al. (1992), and the coefficient of restitution is independent of the body properties.

<sup>12</sup> The suction parameter provides a simple means of adding soil suction to a representative volume of material at a grain-grain contact. A similar quantity, denoted as effective pressure, is defined in Potyondy and Emam (2008&2009), wherein suction behavior is modeled by adding capillary pressure-induced suction forces within a synthetic material consisting of circular particles bonded at their contact points. The representative volume in both the P&E and hill materials consists of two particles and their contact. In the P&E material, we define the capillary pressure as the average pressure in all voids in the representative volume, and note that capillary pressure varies with saturation. We then consider a surface that cuts through this volume, and note that the portion of the surface area that intersects the pore water in the voids is proportional to the saturation; thus, the effective pressure acting on the surface ( $P_e$ ) is given by the product of the saturation and capillary pressure. As the saturation approaches zero, the capillary pressure approaches infinity, but the effective pressure is finite. The moisture force at a P&E contact is found by multiplying the effective pressure ( $P_e$ ) by the cross section of the contact. The maximum moisture force at a hill contact is found by multiplying the suction ( $\psi$ ) by the cross section of the contact shown in Figure 6. In the P&E model, the effective pressure is an internal variable equal to the product of saturation and capillary pressure, with the capillary pressure given by an empirical law of the van Genuchten form. In the hill model, the suction is a model parameter estimated from the empirical relationships of Gupta and co-workers (Gupta and Larson, 1979; Gupta et al., 2005&2007).

and  $g_m$  is the moisture gap. After this function has been invoked, the wet hill contact model with suction  $\psi$  will exist between all grains that are within the moisture-gap distance of one another.<sup>13</sup>

When using the hill material to represent a typical aggregate base of a pavement system, the sand- and finer-sized particles in the grain-size distribution of the physical material are often excluded from the model in order to reduce the number of particles and their associated computational expense. The absence of these fine particles is accounted for by use of a positive moisture gap, which extends the application of the suction to particles separated by this gap, and thereby accounts for the suction produced by the fine particles that partially fill the voids between the coarse particles in the modeled system. The friction coefficient may also be reduced to account for the stabilizing or lubricating effect of the fine particles between the coarse particles in the modeled system.

## 1.5 Activity-Deletion Criteria

A contact with the hill model is active if it is wet ( $M = 2$ ) or if the contact gap is less than or equal to zero. The force-displacement law is skipped for inactive contacts.

## 1.6 Force-Displacement Law

The force-displacement law for the hill model updates the contact force and moment:

$$\mathbf{F}_c = \mathbf{F}^s + \mathbf{F}^m, \quad \mathbf{M}_c \equiv \mathbf{0} \quad (7)$$

where  $\mathbf{F}^s$  is the surface-interaction force and  $\mathbf{F}^m$  is the moisture force. The surface-interaction force consists of Hertzian and dashpot components with the Hertz-Mindlin springs acting in parallel with the dashpots:

$$\mathbf{F}^s = \mathbf{F}^h + \mathbf{F}^d. \quad (8)$$

The surface-interaction force is resolved into a normal and shear force:

$$\mathbf{F}^s = -F_n^s \hat{\mathbf{n}}_c + \mathbf{F}_s \quad (9)$$

where  $F_n^s > 0$  is tension. The shear force lies on the contact plane and is expressed in the contact plane coordinate system:

---

<sup>13</sup> This operation may create new grain-grain contacts, and such contacts will be assigned the wet hill contact model with suction  $\psi$ . The new grain-grain contacts are created between grains that are within the moisture-gap distance of one another. Note that there are many grains in a typical granular assembly that are near to one another, but contacts may not exist between all of these near-neighbor pairs.

$$\mathbf{F}_s = F_{ss} \hat{\mathbf{s}}_c + F_{st} \hat{\mathbf{t}}_c. \quad (10)$$

The moisture force acts in the normal direction:

$$\mathbf{F}^m = -F^m \hat{\mathbf{n}}_c \quad (11)$$

where  $F^m > 0$  is tension (suction) and  $F^m \geq 0$ .

The force-displacement law for the hill model consists of the following steps (see Figure 5 and properties in Section 1.7).

1. Update  $F^m$  as follows (see Figure 6). If the contact is dry ( $M \neq 2$ ), then  $F^m = 0$ ; otherwise, set

$$F^m = \begin{cases} F_{\max}^m, & g_c < 0 \\ F_{\max}^m \exp\left(\frac{-g_c}{2s_{cr}}\right), & 0 \leq g_c \leq 2s_{cr} \\ 0, & g_c > 2s_{cr} \end{cases}$$

with  $F_{\max}^m = \psi(\pi R_o^2)$

$$s_{cr} = R_o = \min(R_1, R_2) \quad (12)$$

where  $R_p$  is the radius of piece ( $p$ ). If the contact is wet and  $g_c > 2s_{cr}$ , then rupture the liquid bridge by setting  $M = 1$ .

2. Update the normal surface-interaction force:

$$F_n^s = F_n^h + F_n^d = \begin{cases} -\tilde{k}_n \delta_o^{3/2} - \tilde{\eta}_n \delta_o^{1/4} \dot{\delta}_o, & \delta_o > 0 \\ 0, & \delta_o \leq 0 \end{cases} \quad (13)$$

with  $\delta_o = -g_c$

where  $\delta_o$  is the contact overlap ( $\delta_o > 0$  is overlap) and  $\dot{\delta}_o$  is the relative translational velocity normal to the contact plane defined such that  $\dot{\delta}_o > 0$  is increasing overlap.

3. Update the shear force ( $\mathbf{F}_s$ ) as follows (see Figure 7). Compute the shear strength:

$$F_s^\mu = -\mu F_n^s. \quad (14)$$

Compute a trial Hertz-Mindlin shear force:

$$\left(\mathbf{F}_s^h\right)^* = \left(\mathbf{F}_s^h\right)_o - \tilde{k}_s \delta_o^{1/2} \dot{\mathbf{d}}_s \Delta t \quad (15)$$

where  $\left(\mathbf{F}_s^h\right)_o$  is the Hertz-Mindlin shear force at the beginning of the time step and  $\dot{\mathbf{d}}_s$  is the relative translational velocity tangential to the contact plane. Update the Hertz-Mindlin shear force (insuring that it lies within the no-slip region):

$$\mathbf{F}_s^h = \begin{cases} \left(\mathbf{F}_s^h\right)^*, & \delta_o > 0 \text{ and } \left\| \left(\mathbf{F}_s^h\right)^* \right\| \leq F_s^\mu \\ F_s^\mu \hat{\mathbf{s}}^h, & \delta_o > 0 \text{ and } \left\| \left(\mathbf{F}_s^h\right)^* \right\| > F_s^\mu \\ 0, & \delta_o \leq 0 \end{cases} \quad (16)$$

with  $\hat{\mathbf{s}}^h = \left(\mathbf{F}_s^h\right)^* / \left\| \left(\mathbf{F}_s^h\right)^* \right\|$ .

Compute a trial shear force:

$$\mathbf{F}_s^* = \mathbf{F}_s^h + \mathbf{F}_s^d \quad (17)$$

with  $\mathbf{F}_s^d = -\tilde{\eta}_s \delta_o^{1/4} \dot{\mathbf{d}}_s$ .

Update the shear force (insuring that it lies within the no-slip region):

$$\mathbf{F}_s = \begin{cases} \mathbf{F}_s^*, & \delta_o > 0 \text{ and } \left\| \mathbf{F}_s^* \right\| \leq F_s^\mu \\ F_s^\mu \hat{\mathbf{s}}, & \delta_o > 0 \text{ and } \left\| \mathbf{F}_s^* \right\| > F_s^\mu \\ 0, & \delta_o \leq 0 \end{cases} \quad (18)$$

with  $\hat{\mathbf{s}} = \mathbf{F}_s^* / \left\| \mathbf{F}_s^* \right\|$ .

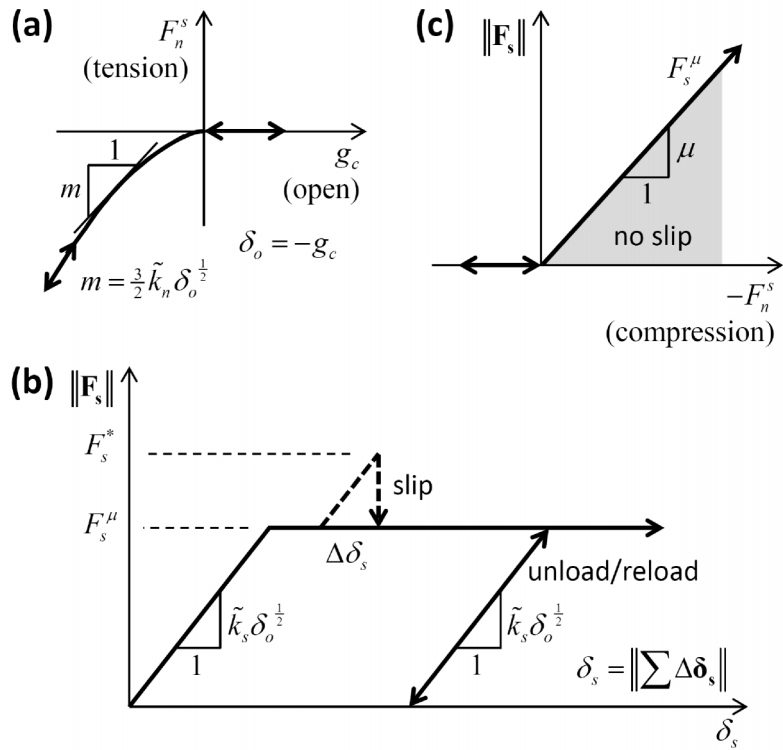


**Figure 5** Force-displacement law for the dry hill model with inactive dashpots:  
(a) normal force versus contact gap, (b) shear force versus relative shear displacement and (c) slip envelope.

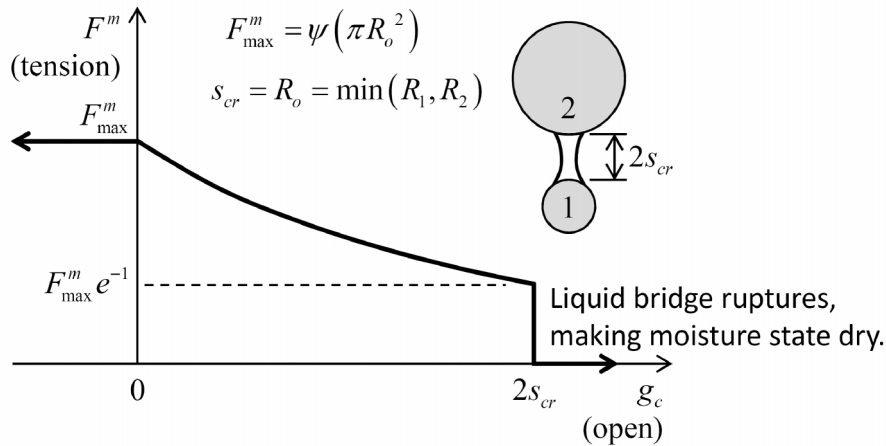


**Figure 6** Moisture force versus contact gap for the wet hill model.

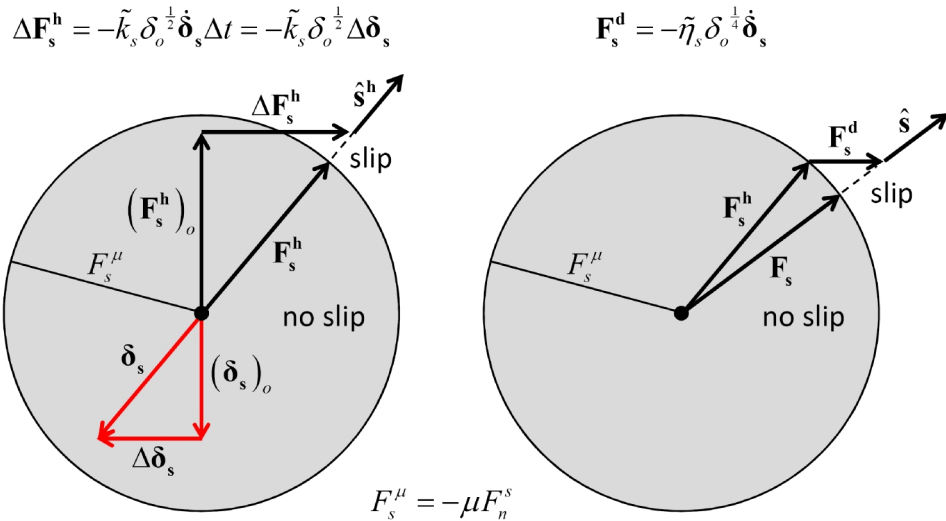


**Figure 7** *Update of the Hertz-Mindlin shear force and relative shear displacement (left) and shear force (right) of the hill model.*

## 1.7 Properties

The property information is separated into parameters and state variables such that the parameters define the model, while the state variables describe its current state. The properties table provides a concise property reference that combines the parameters and state variables. The property information for the hill model is given in Tables 3 to 5. For the first mapping in Table 4:  $R_e$ ,  $E_e$  and  $G_e$  are the effective radius, Young's modulus and shear modulus, respectively, of the contact;  $R_p$  is the radius of piece ( $p$ ) ; and  $E_b$  and  $\nu_b$  are the Young's modulus and Poisson's ratio, respectively, of body ( $b$ ) . For the second mapping in Table 4:  $m_e$  is the effective mass of the contact, and  $m_b$  is the mass of body ( $b$ ) .

**Table 3 Hill Model Parameters**

Parameter	Keyword	Description
	hill	model name
<b>Associated with contacts:</b>		
$\mu$	fric_coef	friction coefficient
$\psi$	suction	suction
$\alpha_h$	damp_con	damping constant
<b>Associated with grains:</b>		
$E_b$	young_mod	Young's modulus of body ( $b$ )

$\nu_b$	<b>pois_ratio</b>	Poisson's ratio of body ( $b$ )
---------	-------------------	---------------------------------

**Table 4 Hill Model State Variables**

Variable	Keyword	Description
$\tilde{k}_n$	<b>nstiff_coef</b>	normal stiffness coeff. $\left[ \text{N} \cdot \text{m}^{-\frac{3}{2}} \right]$
$\tilde{k}_s$	<b>sstiff_coef</b>	shear stiffness coeff. $\left[ \text{N} \cdot \text{m}^{-\frac{3}{2}} \right]$
<b>Mapping:</b>		
		$\tilde{k}_n = \frac{4}{3} E_e \sqrt{R_e}, \quad \tilde{k}_s = 8G_e \sqrt{R_e}; \quad R_e = \left( \frac{1}{R_1} + \frac{1}{R_2} \right)^{-1}$ $E_e = \left( \frac{1 - \nu_1^2}{E_1} + \frac{1 - \nu_2^2}{E_2} \right)^{-1}, \quad G_e = \left( \frac{2(1 + \nu_1)(2 - \nu_1)}{E_1} + \frac{2(1 + \nu_2)(2 - \nu_2)}{E_2} \right)^{-1}$
$\tilde{\eta}_n$	<b>ndamp_coef</b>	normal damping coeff. $\left[ \text{kg} \cdot \text{m}^{-\frac{1}{4}} \cdot \text{s}^{-1} \right]$
$\tilde{\eta}_s$	<b>sdamp_coef</b>	shear damping coeff. $\left[ \text{kg} \cdot \text{m}^{-\frac{1}{4}} \cdot \text{s}^{-1} \right]$
<b>Mapping:</b>		
		$\tilde{\eta}_n = \alpha_h \sqrt{m_e \tilde{k}_n}, \quad \tilde{\eta}_s = \alpha_h \sqrt{m_e \tilde{k}_s}; \quad m_e = \left( \frac{1}{m_1} + \frac{1}{m_2} \right)^{-1}$
$\delta_o$	<b>overlap</b>	contact overlap ( $\delta_o > 0$ is overlap)
		moisture state
$M$	<b>mois_state</b>	$\begin{cases} 0, \text{ dry} \\ 1, \text{ dry \& ruptured} \\ 2, \text{ wet} \end{cases}$
$F^s$	<b>surf_force</b>	surface-interaction force $(-F_n^s, F_{ss}, F_{st})$ where $F_n^s > 0$ is tension
$F^m$	<b>mois_force</b>	moisture force ( $F^m$ ) where $F^m > 0$ is tension (suction)

**Table 5 Hill Model Properties**

Keyword	Symbol	Range	Default	Type	Modifiable
<b>fric_coef</b>	$\mu$	$[0.0, \infty)$	0.0	FLT	yes
<b>suction</b>	$\psi$	$[0.0, \infty)$	0.0	FLT	yes
<b>damp_con</b>	$\alpha_h$	$[0.0, 1.0]$	0.0	FLT	yes
<b>young_mod</b>	$E_b$	$[0.0, \infty)$	0.0	FLT	no <sup>+</sup>
<b>pois_ratio</b>	$\nu_b$	$(-1.0, 0.5]$	0.0	FLT	no <sup>+</sup>
<b>nstiff_coef</b>	$\tilde{k}_n$	$[0.0, \infty)$	0.0	FLT	no
<b>sstiff_coef</b>	$\tilde{k}_s$	$[0.0, \infty)$	0.0	FLT	no
<b>ndamp_coef</b>	$\tilde{\eta}_n$	$[0.0, \infty)$	0.0	FLT	no
<b>sdamp_coef</b>	$\tilde{\eta}_s$	$[0.0, \infty)$	0.0	FLT	no
<b>overlap</b>	$\delta_o$	$\mathbb{R}$	NA	FLT	no
<b>mois_state</b>	$M$	$\{0, 1, 2\}$	0	INT	no (set via methods)
<b>surf_force</b>	$\mathbf{F}^s$	$[\mathbb{R}, \mathbb{R}, \mathbb{R}]$	$\mathbf{0}$	VEC3	no
<b>mois_force</b>	$F^m$	$[0.0, \infty)$	0.0	FLT	no

<sup>+</sup> Surface property of a body (ball or clump).

## 1.8 Methods

**Table 6 Hill Model Methods**

Method	Argument	Description
<b>make_wet</b>		Add moisture if $g_c \leq g_m$ .
	<b>gap</b>	moisture gap ( $g_m$ )
<b>make_dry</b>		Remove moisture.

**make\_wet.** Add moisture if the contact gap between the pieces is less than or equal to the moisture gap.<sup>14</sup> If moisture is added, then the moisture state becomes wet ( $M = 2$ ) — the moisture force is unaffected and will be updated during the next cycle.

**make\_dry.** Remove moisture. The moisture state becomes dry ( $M = 0$ ) — the moisture force is unaffected and will be updated during the next cycle.

## 1.9 Time Step Estimation Scheme

The procedure to compute a stable time step in *PFC3D* 4.0 (see Section 1.6 in the Theory & Background volume of Itasca [2008]) requires that each contact model return the contact translational and rotational stiffnesses. For the hill model, the rotational stiffnesses are zero ( $k_t = k_b \equiv 0$ ), and the translational stiffnesses are

$$k_n = \frac{3}{2} \tilde{k}_n \delta_o^{\frac{1}{2}}, \quad k_s = \tilde{k}_s \delta_o^{\frac{1}{2}} \quad (19)$$

where  $\delta_o$  is the contact overlap. If  $\delta_o \leq 0$  (which may occur when the contact is wet), then we return the stiffnesses that correspond with  $\delta_o = (2.0 \times 10^{-4}) R_o$ , with  $R_o$  given by Eq. (12). If the contact model includes dashpots, then the translational stiffnesses must be increased via

$$\begin{aligned} k_n &:= k_n / F(\beta_n)^2, \quad k_s := k_s / F(\beta_s)^2 \\ F(\xi) &= \sqrt{1 + \xi^2} - \xi, \quad 0 \leq \xi \leq 1 \end{aligned} \quad (20)$$

where  $\beta_n$  and  $\beta_s$  are the critical damping ratios in the normal and shear directions, respectively. It may be possible to express the critical damping ratios in terms of the damping constant ( $\alpha_h$ ) and the contact overlap by analyzing the equation of motion for a fixed particle in contact with a free particle via the hill contact model.<sup>15</sup> Time limitations preclude the analysis from being done; therefore, we assume that the following relation holds:

$$\beta_n = \beta_s = \frac{\alpha_h}{2} \quad (21)$$

<sup>14</sup> One can ensure the existence of contacts between all pieces with a contact gap less than a specified moisture gap ( $g_m$ ) by adding moisture to the material via the **hlm\_makeWet** FISH function.

<sup>15</sup> The analysis will be similar to the analysis of Tsuji et al. (1992) in their derivation of the relationship between damping constant and coefficient of restitution.

and increase the translational stiffnesses via Eq. (20). It is expected that this will be sufficient for models that have small values of damping constant ( $\alpha_h \leq 0.1$ ).<sup>16</sup>

## 2.0 TEST PROBLEMS

The pavement-design package provides the hill contact model, and supports creation of a hill material that can be subjected to triaxial testing. Test problems of two granite grains, and an assembly of granite grains are provided in the following subsections. An example of a hill material is provided in Potyondy (2016, User-Defined Material Example). There is a *PFC3D* project for each test problem, and these projects are in the **fistPkgN/ExampleProjects/..**

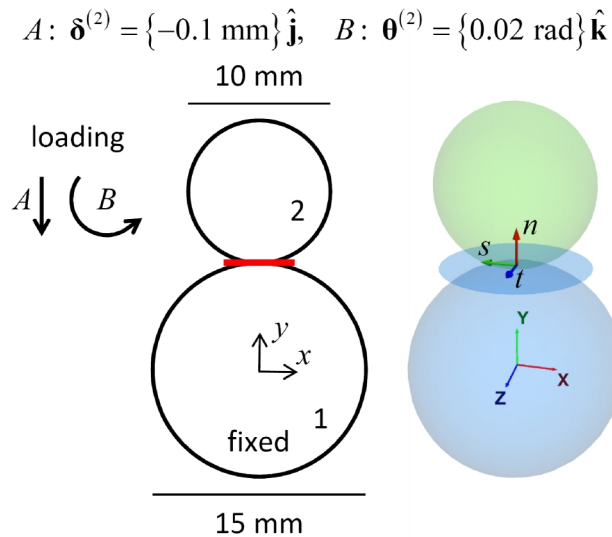
**HillContactModel** directory, where **N** is the version number of the material-modeling support package.

### 2.1 Two Granite Grains

The two-grain test problem is in the **Test-TwoGraniteGrains** example-project directory. The problem is shown in Figure 8 and described as follows. Two granite grains are stacked one atop the other. The bottom grain is fully fixed. The top grain is (A) moved down by 0.1 mm, and then (B) rotated by 0.02 radians. The granite grains are gravel-sized spheres with diameters ranging from 10–25 mm.

---

<sup>16</sup> The damping constant used in all of the simulations performed by Tan et al. (2014a) was 0.07 (as stated in their Appendix A), which corresponds with a restitution coefficient of 0.9. The damping constant is set to zero and local damping (with a local-damping factor of 0.7) is used when simulating quasi-static triaxial testing of the hill material.



$$\Delta\delta_n = -0.1 \text{ mm}, \quad \Delta\delta_{ss} = -99.0 \mu\text{m}, \quad \Delta\delta_{st} = 0 \\ \Delta\theta_t = 0, \quad \Delta\theta_{bs} = 0, \quad \Delta\theta_{bt} = 0.02 \text{ rad}$$

**Figure 8 Two-grain test problem.**

The two-grain test problem is modeled with both the linear and hill contact models. The material properties are summarized in Figure 9 and described as follows. The density, Young's modulus and Poisson's ratio of granite are  $2650 \text{ kg/m}^3$ , 29 GPa and 0.15, respectively. The friction coefficient is 0.4. The suction of the hill model is 200 kPa. We enforce quasi-static conditions via local-damping, with a local-damping factor of 0.7. Additional damping is applied to the hill model via a damping constant of 0.07, which corresponds with a 0.9 coefficient of restitution.

**granite**

$$\rho = 2650 \text{ kg/m}^3, E = 29 \text{ GPa}, \nu = 0.15$$

$$\mu = 0.4$$

**linear model:**

grain density, effective modulus, stiffness ratio, friction coefficient

local-damping factor

$$\rho_g = 2650 \text{ kg/m}^3, \{E^* = 29 \text{ GPa}, \kappa^* = 1.0\}$$

$$\mu = 0.4, \alpha = 0.7 \quad \{k_n = k_s\} = 1.8221 \times 10^8 \text{ N/m}$$

**hill model:**

Young's modulus, Poisson's ratio and density of each grain

friction coefficient, suction, damping constant, local-damping factor

$$E_g = 29 \text{ GPa}, \nu_g = 0.15, \rho_g = 2650 \text{ kg/m}^3, \mu = 0.4, \psi = 200 \text{ kPa}$$

$$\alpha_h = 0.07, \alpha = 0.7$$

**Figure 9 Material properties of the two-grain test problem.**

The force-displacement response of the linear model is shown in Figure 10. The normal force at the end of loading-stage B is given by

$$F_n = k_n g_c = \{1.8221 \times 10^8 \text{ N/m}\} \{-0.1 \times 10^{-3} \text{ m}\} = -1.8221 \times 10^4 \text{ N.} \quad (22)$$

The shear force at the end of loading-stage B is given by

$$\begin{aligned} F_{ss}^* &= -k_s \Delta \delta_{ss}, \quad F_{st}^* = -k_s \Delta \delta_{st} = 0 \\ &= -\{1.8221 \times 10^8 \text{ N/m}\} \{-99.0 \mu\text{m}\} = 1.8039 \times 10^4 \text{ N} \\ F_s^\mu &= -\mu F_n \\ &= -\{0.4\} \{-1.8221 \times 10^4 \text{ N}\} = 7.2884 \times 10^3 \text{ N} \\ F_{ss} &= 7.2884 \times 10^3 \text{ N, } F_{st} = 0. \end{aligned} \quad (23)$$

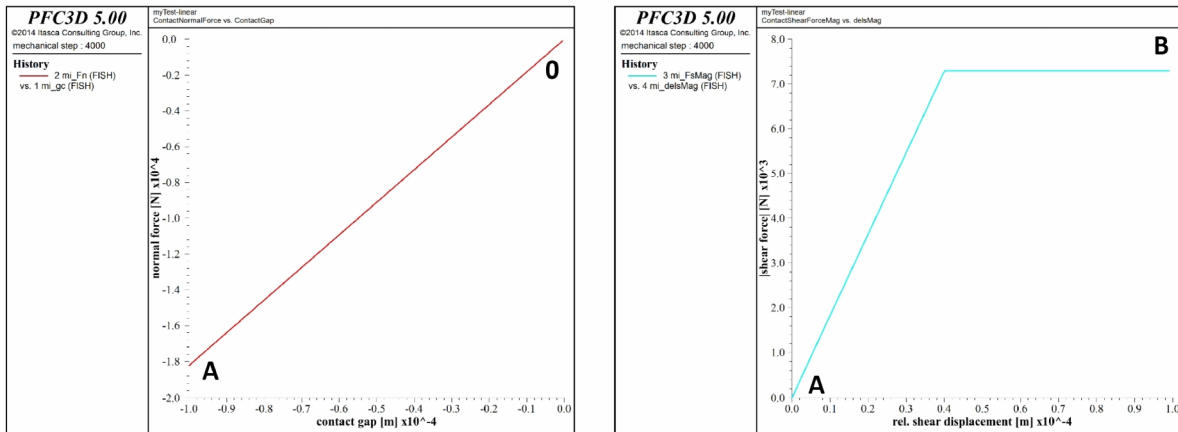
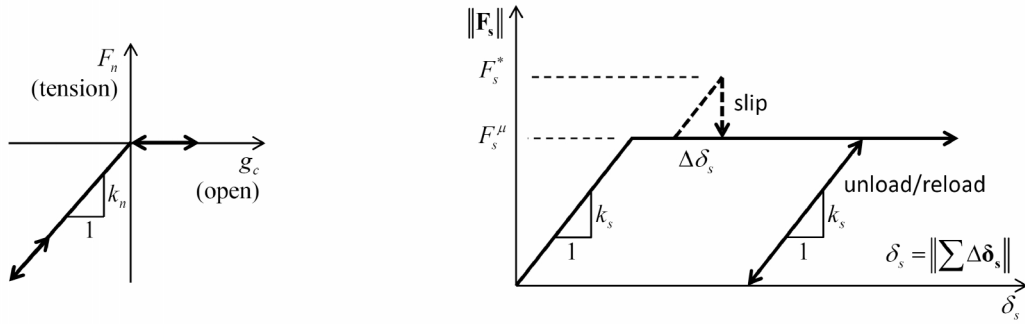


**Figure 10** Force-displacement response of the linear model: normal force versus contact gap (left) and shear force versus relative shear displacement (right).

The force-displacement response of the hill model is shown in Figure 11. The normal force at the end of loading-stage B is given by

$$\begin{aligned}
 E_e &= \left( \frac{1-v_1^2}{E_1} + \frac{1-v_2^2}{E_2} \right)^{-1} = \left( \frac{2(1-\{0.15\}^2)}{29 \text{ GPa}} \right)^{-1} = 14.834 \text{ GPa} \\
 R_e &= \left( \frac{1}{R_1} + \frac{1}{R_2} \right)^{-1} = \left( \frac{1}{7.5 \text{ mm}} + \frac{1}{5.0 \text{ mm}} \right)^{-1} = 3.0 \text{ mm} \\
 \tilde{k}_n &= \frac{4}{3} E_e \sqrt{R_e} = \frac{4}{3} \{14.834 \times 10^9 \text{ N/m}^2\} \sqrt{3.0 \times 10^{-3} \text{ m}} = 1.0833 \times 10^9 \text{ N} \cdot \text{m}^{-\frac{3}{2}} \\
 F_n^s &= F_n^h + F_n^d = -\tilde{k}_n \delta_o^{\frac{3}{2}} + 0 = -\{1.0833 \times 10^9 \text{ N} \cdot \text{m}^{-\frac{3}{2}}\} \{0.1 \times 10^{-3} \text{ m}\}^{\frac{3}{2}} = -1.0833 \times 10^3 \text{ N}.
 \end{aligned} \tag{24}$$

The shear force at the end of loading-stage B is given by

$$\begin{aligned}
 G_e &= \left( \frac{2(1+\nu_1)(2-\nu_1)}{E_1} + \frac{2(1+\nu_2)(2-\nu_2)}{E_2} \right)^{-1} \\
 &= \left( \frac{4(1+0.15)(2-0.15)}{29 \text{ GPa}} \right)^{-1} = 3.4078 \text{ GPa} \\
 R_e &= \left( \frac{1}{R_1} + \frac{1}{R_2} \right)^{-1} = \left( \frac{1}{7.5 \text{ mm}} + \frac{1}{5.0 \text{ mm}} \right)^{-1} = 3.0 \text{ mm} \\
 \tilde{k}_s &= 8G_e\sqrt{R_e} = 8\{3.4078 \times 10^9 \text{ N/m}^2\}\sqrt{3.0 \times 10^{-3} \text{ m}} = 1.4932 \times 10^9 \text{ N} \cdot \text{m}^{-\frac{3}{2}} \\
 (\mathbf{F}_{ss}^h)^* &= -\tilde{k}_s \delta_o^{\frac{1}{2}} \Delta \delta_{ss}, \quad (\mathbf{F}_{st}^h)^* = -\tilde{k}_s \delta_o^{\frac{1}{2}} \Delta \delta_{st} = 0 \quad (25) \\
 &= -\{1.4932 \times 10^9 \text{ N} \cdot \text{m}^{-\frac{3}{2}}\} \{0.1 \times 10^{-3} \text{ m}\}^{\frac{1}{2}} \{-99.0 \mu\text{m}\} = 1.4783 \times 10^3 \text{ N} \\
 F_s^\mu &= -\mu F_n^s \\
 &= -\{0.4\} \{-1.0833 \times 10^3 \text{ N}\} = 4.3332 \times 10^2 \text{ N} \\
 \mathbf{F}_{ss} &= 4.3332 \times 10^2 \text{ N}, \quad \mathbf{F}_{st} = 0.
 \end{aligned}$$

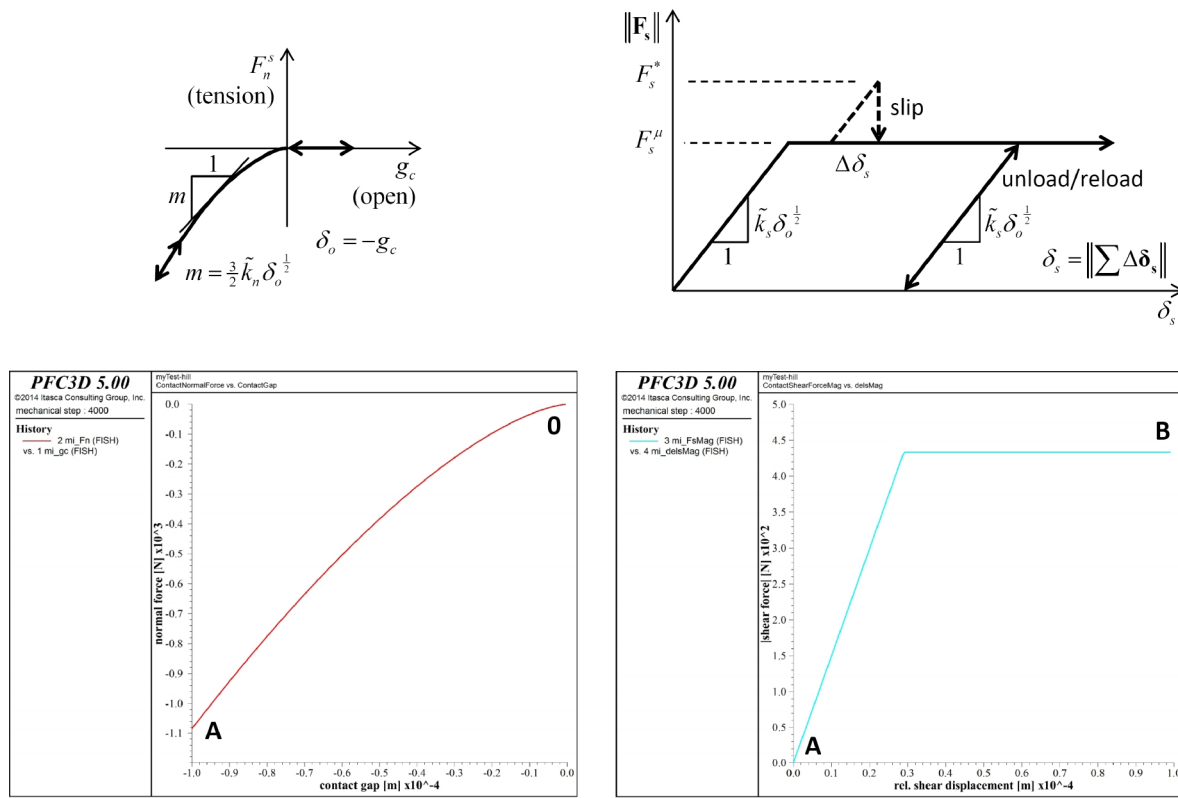


**Figure 11 Force-displacement response of the dry hill model with inactive dashpots: normal force versus contact gap (left) and shear force versus relative shear displacement (right).**

The linear model produces a much stiffer response than the hill model (see Figure 12). This is not surprising. The effective modulus of the linear model (and its corresponding normal stiffness) was set equal to that of granite, and this normal stiffness remains constant with increasing overlap, whereas the normal stiffness of the hill model increases with increasing overlap. The normal force of the hill model lags behind that of the linear model, and the stiffnesses (given by the slopes) become equal when the overlap reaches 12.5 mm. The normal force of the hill model finally exceeds that of the linear model when the overlap reaches 28.2 mm. The radius of the smaller grain is 5.0 mm, and thus, overlaps greater than 2.0 mm are unacceptable, because the overlap must remain small relative to the grain size for the soft-contact approach of the PFC model, in which all deformation occurs at the contacts between the rigid grains, to be valid. The behavior observed here will help guide the choice of properties for the linear and hill materials. There is a fundamental difference between the two models in that the linear model has a constant stiffness whereas the hill model has a stiffness that increases with increasing overlap. It is expected that the macroscopic modulus of a hill material will be more sensitive to confining pressure than that of a linear material.

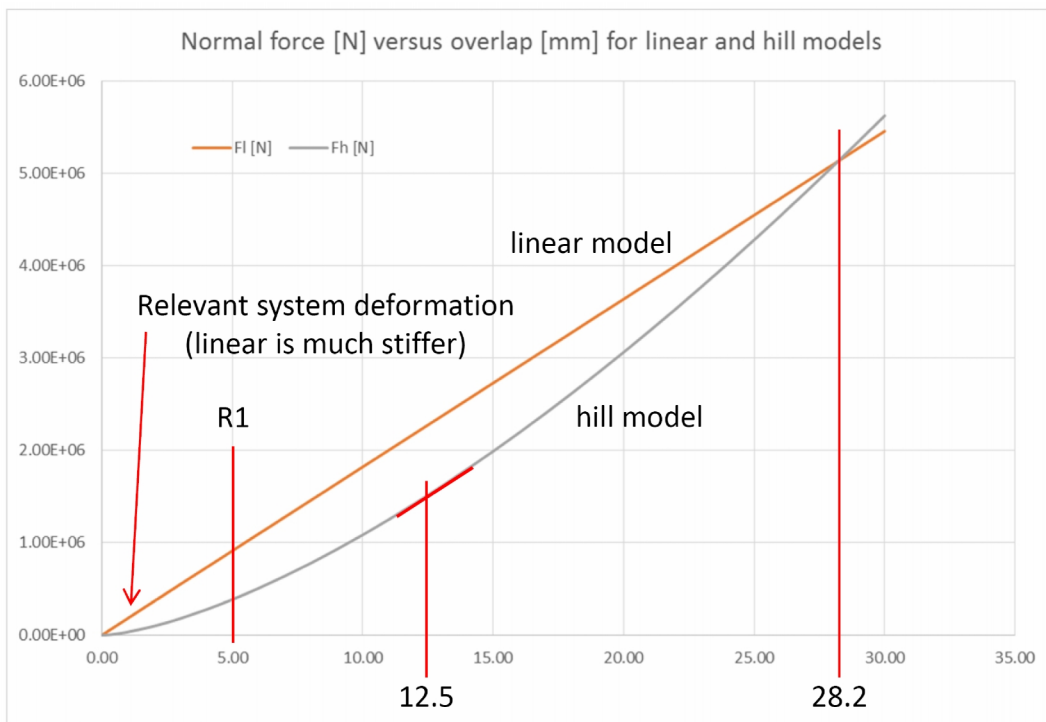


**Figure 12 Normal force versus overlap for the linear and hill models.**

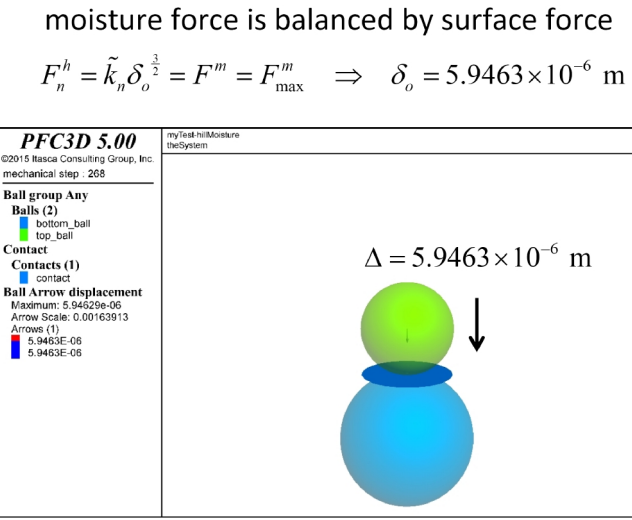
We study the effect of the dashpots on the force-displacement response of the hill model as follows. We set the damping constant equal to zero (to insure that the normal and shear forces at the end of loading-stage B are not affected by the dashpots), and rerun the model to reach the end of loading-stage B. We then set the damping constant equal to 0.07, and move the top grain down at a velocity of 100 m/s for one time step (thereby increasing the overlap to 0.2 mm) and also increasing the normal force to  $3.9604 \times 10^3$  N. Setting the velocity of the top grain to zero reduces the normal force to  $3.0640 \times 10^3$  N. The computations that give these values are given by

$$\begin{aligned}
 m_1 &= \rho \left( \frac{4}{3} \pi R_1^3 \right) = \left\{ 2650 \frac{\text{kg}}{\text{m}^3} \right\} \left( \frac{4}{3} \pi \left\{ 7.5 \times 10^{-3} \text{ m} \right\}^3 \right) = 4.6829 \times 10^{-3} \text{ kg} \\
 m_2 &= \rho \left( \frac{4}{3} \pi R_2^3 \right) = \left\{ 2650 \frac{\text{kg}}{\text{m}^3} \right\} \left( \frac{4}{3} \pi \left\{ 5.0 \times 10^{-3} \text{ m} \right\}^3 \right) = 1.3875 \times 10^{-3} \text{ kg} \\
 m_e &= \left( \frac{1}{m_1} + \frac{1}{m_2} \right)^{-1} = 1.0704 \times 10^{-3} \text{ kg} \\
 \tilde{\eta}_n &= \alpha_h \sqrt{m_e \tilde{k}_n} = \{0.07\} \sqrt{\{1.0704 \times 10^{-3} \text{ kg}\} \{1.0833 \times 10^9 \text{ N} \cdot \text{m}^{-\frac{3}{2}}\}} = 75.378 \text{ kg} \cdot \text{m}^{-\frac{1}{4}} \cdot \text{s}^{-1} \quad (26) \\
 \mathbf{F}_n^s &= \mathbf{F}_n^h + F_n^d = -\tilde{k}_n \delta_o^{\frac{3}{2}} - \tilde{\eta}_n \delta_o^{\frac{1}{4}} \dot{\delta}_o = -\left\{ 1.0833 \times 10^9 \text{ N} \cdot \text{m}^{-\frac{3}{2}} \right\} \left\{ 0.2 \times 10^{-3} \text{ m} \right\}^{\frac{3}{2}} - \\
 &\quad \left\{ 75.378 \text{ kg} \cdot \text{m}^{-\frac{1}{4}} \cdot \text{s}^{-1} \right\} \left\{ 0.2 \times 10^{-3} \text{ m} \right\}^{\frac{1}{4}} \{100 \text{ m/s}\} = \{-3.0640 \times 10^3 \text{ N}\} - \{896.40 \text{ N}\} \\
 &= -3.9604 \times 10^3 \text{ N}.
 \end{aligned}$$

We set the damping constant to zero (to insure that the normal and shear forces at the end of loading-stage B are not affected by the dashpots), the friction coefficient to 1000 (so that the shear force is not limited by the shear strength), and rerun the model to reach the end of loading-stage B, at which point the shear force is  $1.4783 \times 10^3 \text{ N}$ . We then set the damping constant equal to 0.07, and rotate the top grain at a rotational velocity of 1000 rad/s for one time step (thereby increasing the relative shear displacement to  $103.95 \mu\text{m}$ ) and also increasing the shear force to  $1.5960 \times 10^3 \text{ N}$ . Setting the rotational velocity of the top grain to zero reduces the shear force to  $1.5522 \times 10^3 \text{ N}$ . The computations that give these values are given by

$$\begin{aligned}
 \tilde{\eta}_s &= \alpha_h \sqrt{m_e \tilde{k}_s} = \{0.07\} \sqrt{\{1.0704 \times 10^{-3} \text{ kg}\} \{1.4932 \times 10^9 \text{ N} \cdot \text{m}^{-\frac{3}{2}}\}} \\
 &= 88.497 \text{ kg} \cdot \text{m}^{-\frac{1}{4}} \cdot \text{s}^{-1} \\
 \mathbf{F}_{ss} &= \mathbf{F}_s^h + F_s^d = -\tilde{k}_s \delta_o^{\frac{1}{2}} \Delta \delta_{ss} - \tilde{\eta}_s \delta_o^{\frac{1}{4}} \dot{\delta}_{ss} = \\
 &\quad -\left\{ 1.4932 \times 10^9 \text{ N} \cdot \text{m}^{-\frac{3}{2}} \right\} \left\{ 0.1 \times 10^{-3} \text{ m} \right\}^{\frac{1}{2}} \\
 &\quad \left\{ -99.0 \mu\text{m} + (-1000.0 \text{ rad/s}) (4.95 \times 10^{-3} \text{ m}) (1.0 \times 10^{-6} \text{ s}) \right\} - \\
 &\quad \left\{ 88.497 \text{ kg} \cdot \text{m}^{-\frac{1}{4}} \cdot \text{s}^{-1} \right\} \left\{ 0.1 \times 10^{-3} \text{ m} \right\}^{\frac{1}{4}} \left\{ (-1000.0 \text{ rad/s}) (4.95 \times 10^{-3} \text{ m}) \right\} = \\
 &\quad \{1.5522 \times 10^3 \text{ N}\} + \{43.806 \text{ N}\} = 1.5960 \times 10^3 \text{ N}, \quad \mathbf{F}_{st} = 0. \quad (27)
 \end{aligned}$$

We study the behavior of the moisture model by adding moisture to the two-grain test problem shown in Figure 8, and then allowing the system to reach static equilibrium. At this point, the moisture force is balanced by the surface force (see Figure 13).



$$\left. \begin{array}{l} F_n^s = -15.708 \text{ N (compression)} \\ F^m = 15.708 \text{ N (suction)} \end{array} \right| \quad F_c^n = -F_n^s - F^m = 0$$

**Figure 13 Initial state of the moisture-model test.**

Next, the top ball is moved up to induce a tensile force in the contact, and when the top ball is released, the system returns to its initial state (see Figure 14). If the top ball is moved up a bit more, then the liquid bridge ruptures and the contact is deleted (see Figure 15). The top ball is then moved down until the gap is just less than 2.0 mm. At this point, moisture is added between all grains with a gap less than a moisture gap of 2.5 mm. This operation causes a new contact to be created and made moist so that when the top ball is released, the system returns to its initial state (see Figure 16).

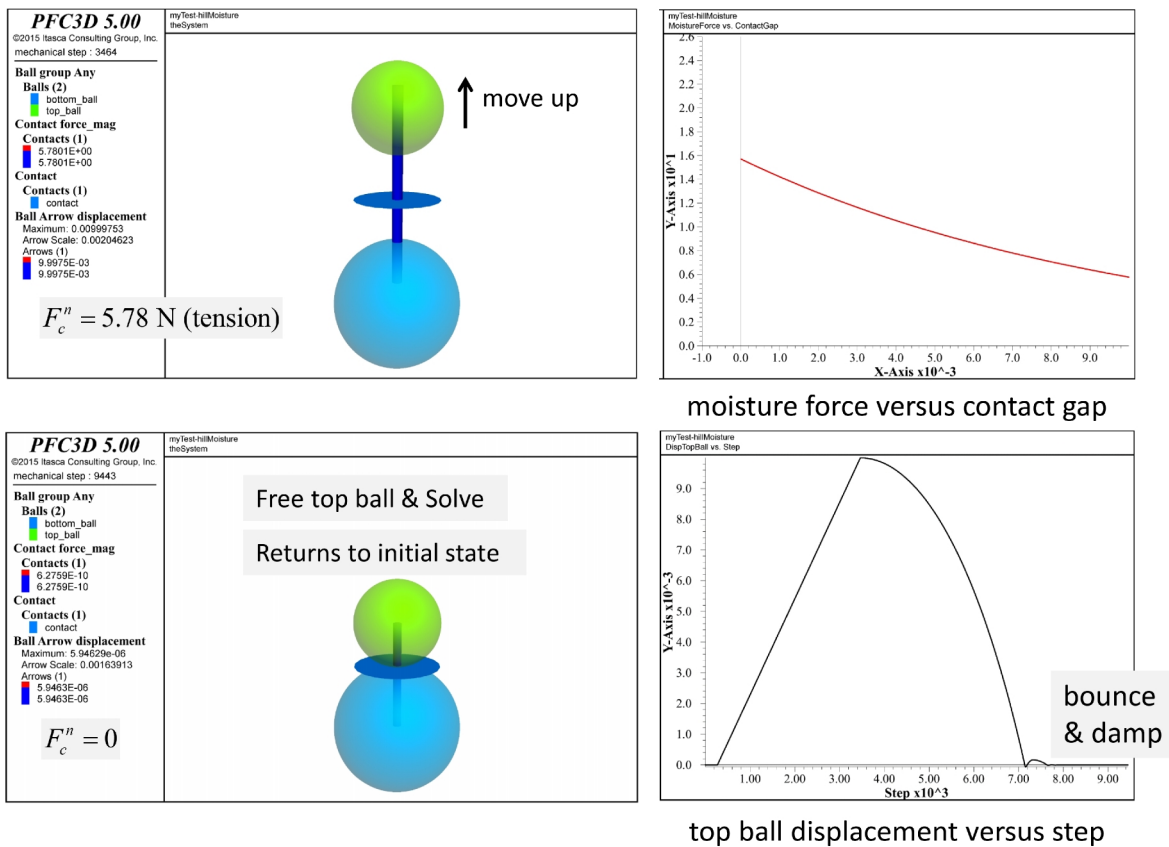


**Figure 14** Moisture-model test in which the top ball is moved up and then released.

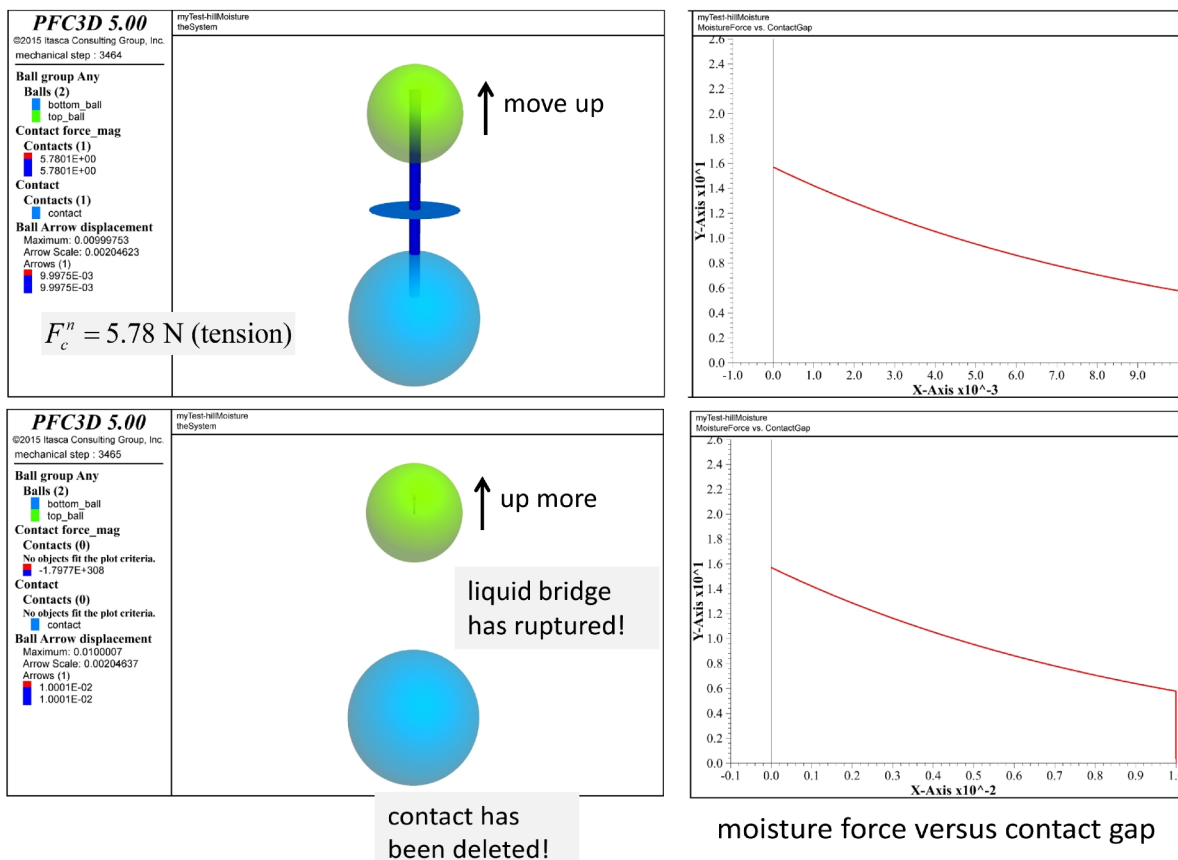
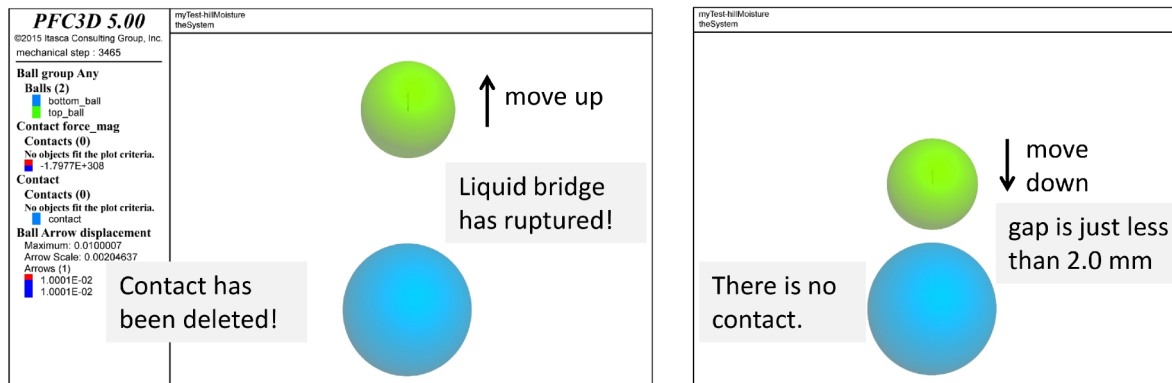


**Figure 15** Moisture-model test in which the top ball is moved up until the liquid bridge ruptures.



Now add moisture between all grains with a gap less than a moisture gap of 2.5 mm.  $g_m = 2.5 \text{ mm}$

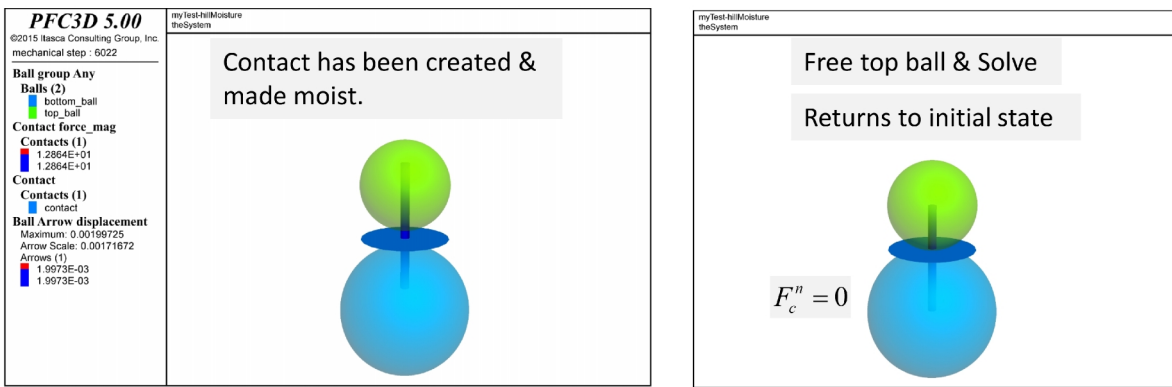


**Figure 16** Moisture-model test in which the top ball is moved up until the liquid bridge ruptures, the top ball is moved down, moisture is added between all grains with a moisture gap less than 2.5 mm and the top ball is released.

## 2.2 Assembly of Granite Grains

The grain-assembly test problem is in the **Test-AssemblyGraniteGrains** example-project directory. The problem is shown in Figure 17 and described as follows. The contact model assignment table (CMAT) is employed to ensure that all ball-ball contacts will be assigned the hill contact model and its associated properties, and all ball-facet contacts will be assigned the linear contact model and its associated properties. The model properties are given in Figure 9, but the effective modulus of the linear model is reduced to 29 MPa. A cubic packing of 27 10-mm diameter balls is generated within the center of a cubic box. Gravity is activated ( $g = 9.81 \text{ m} \cdot \text{s}^{-2}$ ), and the model is allowed to reach static equilibrium. The total force on the bottom wall is found to equal the total weight of the balls ( $W = 27\rho_g\left(\frac{4}{3}\pi R_g^3\right)g = 0.368 \text{ N}$ ).

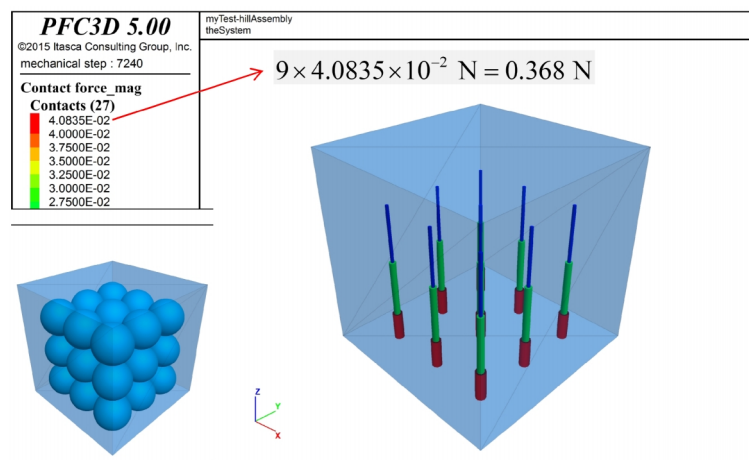


**Figure 17** Grain-assembly test problem showing initial model, and model in static equilibrium after activating gravity.

### 2.3 Material-Behavior Study

The material-behavior study is in the **MatGen-Class5** example-project directory. Linear and hill materials are created to represent a typical aggregate base layer of an asphalt-surface roadway (Potyondy et al., 2016). The aggregate particles are modeled as granite spheres drawn from two grain-size distributions (see Figure 18). The first distribution (denoted as C5n) is narrow, with grain diameters that range from 14 to 20 mm. The second distribution (denoted as C5b) is broad to represent the upper end of the MnDOT Class 5 aggregate base grading designation. The materials are denoted as Class 5 materials with microproperties listed in Table 7. The materials are dry while being created in a cylindrical material vessel (of initial 240-mm height and 170-mm diameter, with a 500 MPa effective modulus) and packed via the boundary-contraction packing procedure at a 150 kPa material pressure as shown in Figure 19. The materials are then subjected to triaxial testing. During each triaxial test, the confinement is 150 kPa, and load-unload cycles are performed at axial strains of 0.02% and 0.05% to measure the resilient moduli (see Figures 20 and 21).<sup>17</sup>

<sup>17</sup> The confinement is similar to that defined in resilient modulus protocols, and axial strains correspond with vertical strains in the aggregate base layer for typical traffic loads.

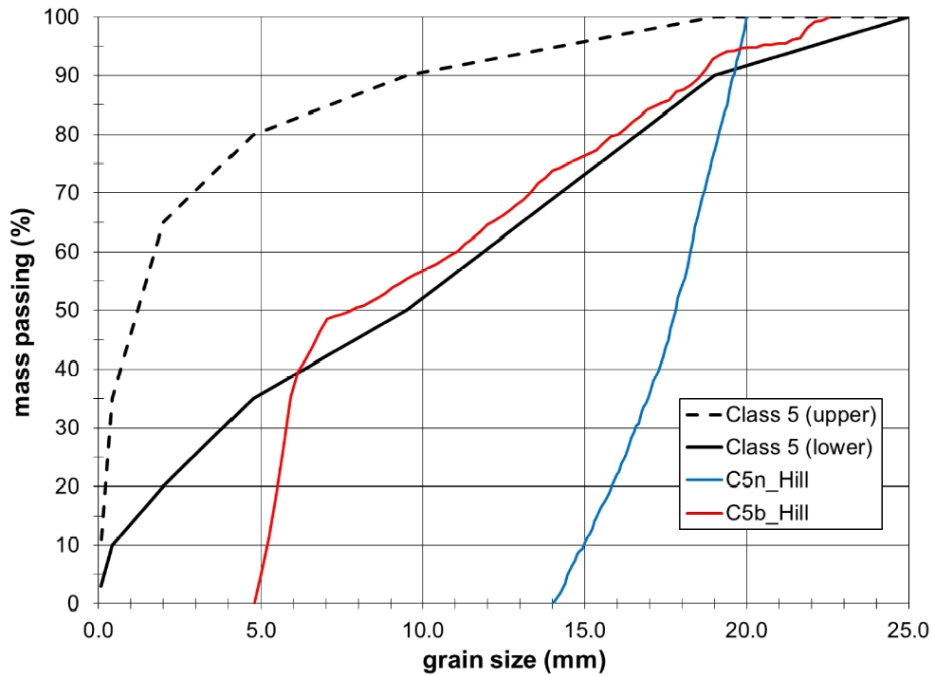


**Figure 18** *Grain size distribution curves for the Class 5 hill materials along with limits of the Class 5 grading designation. The linear materials have similar grain size distribution curves.*

**Table 7** *Microproperties of Class 5 Materials\**

Property	Value
<b>Common group:</b>	
$N_m$	C5{n,b}_Linear,Hill
$T_m$ , $\alpha$ , $C_p$ , $\rho_v$ [ $\text{kg}/\text{m}^3$ ]	{0,4}, 0.7, 0, 2650
$S_g$ , $T_{SD}$ , $D_{mult}$	0, 0, 1.0
$\{D_{\{l,u\}}^{(j)}\}$ [mm], $\phi^{(j)}$	$\left\{ \begin{array}{ll} \{14,20,1.0\}, & \text{C5n} \\ \{\{19.0,23.0,0.07\}^{(1)}, & \{16.5,19.0,0.10\}^{(2)}\} \\ \{14.0,16.5,0.09\}^{(3)}, & \{12.0,14.0,0.09\}^{(4)} \\ \{9.5,12.0,0.09\}^{(5)}, & \{7.0,9.5,0.07\}^{(6)} \\ \{6.0,7.0,0.10\}^{(7)}, & \{4.8,6.0,0.39\}^{(8)} \end{array} \right.$
<b>Packing group:</b>	
$S_{RN}$ , $P_m$ [kPa], $\varepsilon_p$ , $\varepsilon_{lim}$ , $n_{lim}$	10000, 150, $1 \times 10^{-2}$ , $8 \times 10^{-3}$ , $2 \times 10^6$
$C_p$ , $n_c$ , $\mu_{CA}$ , $v_{lim}$ [m/s]	0, 0.58, 0, 1.0
<b>Linear material group (C5{n,b}_Linear):</b>	

$E^*$ [MPa], $\kappa^*$ , $\mu$	500, 1.5, 0.4
<b>Hill material group (C5{n,b}_Hill):</b>	
$E_g$ [GPa], $\nu_g$ , $\mu$ , $\alpha_h$ , $\psi$ [kPa]	29, 0.15, 0.4, 0, 20

\* Linear material parameters are defined in Potyondy (2016), and Hill material parameters are defined in Table 2 of this memo.

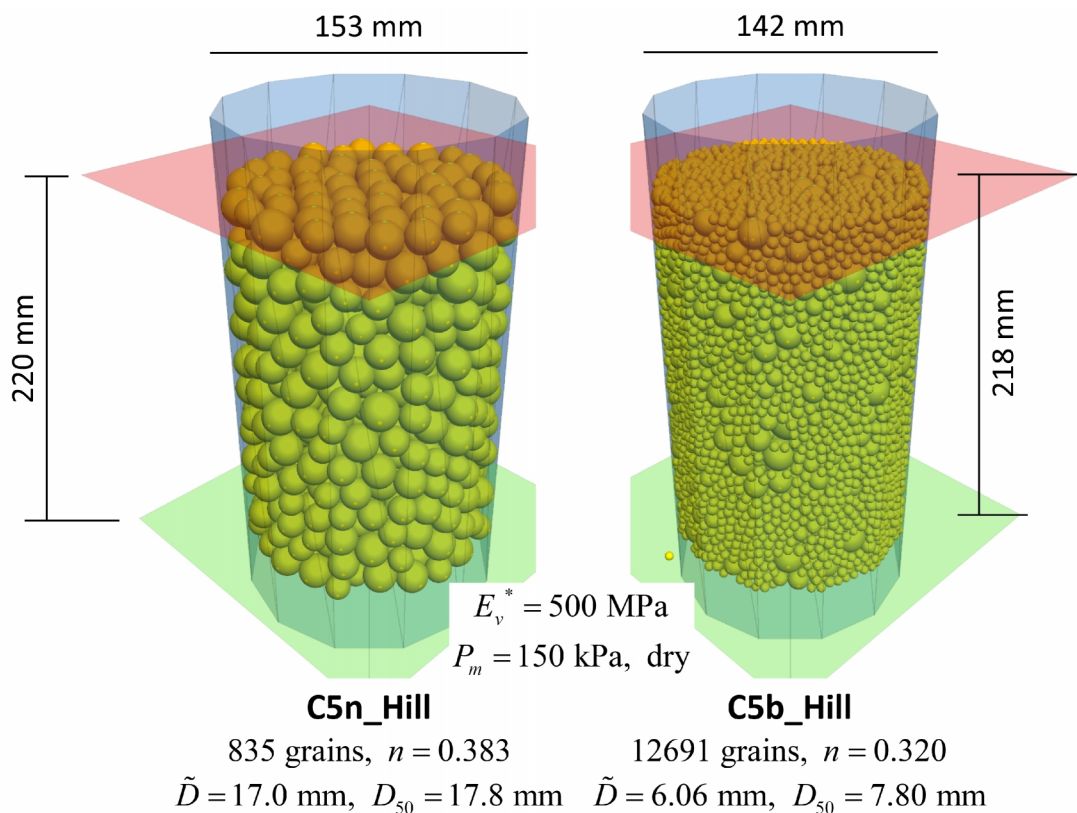


**Figure 19** Class 5 hill materials packed at 150 kPa material pressure at the end of material genesis. The linear materials have similar packing and microstructural properties.

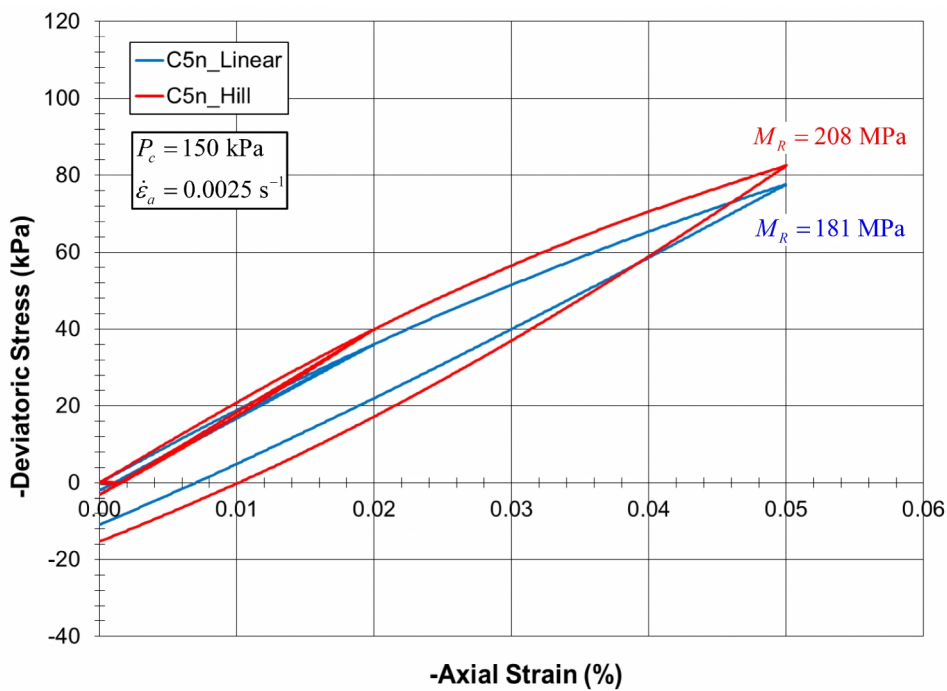


**Figure 20** Deviator stress versus axial strain for Class 5 materials with narrow grain-size distributions tested at 150 kPa confinement.

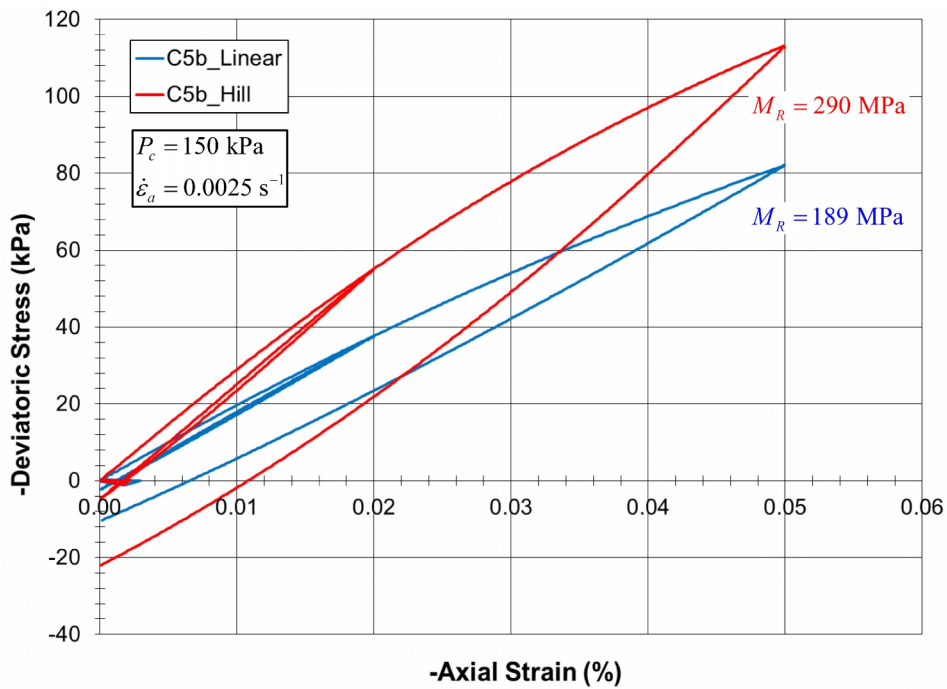


**Figure 21** Deviator stress versus axial strain for Class 5 materials with broad grain-size distributions tested at 150 kPa confinement.

The linear and hill materials differ in the force-displacement response of their respective grain-grain systems. The linear material has linear springs that provide a linear force-displacement response, while the hill material has Hertz-Mindlin springs that provide a nonlinear force-displacement response. The stiffness of the linear springs remains constant, while the stiffness of the Hertz-Mindlin springs increases with increasing overlap. The following conclusions can be drawn from this study.

- The materials with the broad grain-size distribution pack to a lower porosity ( $n = 0.320$ ) than those with the narrow grain-size distribution ( $n = 0.383$ ).
- The stress-strain responses of both materials are similar. There is a hysteretic loop during each load-unload cycle. The size of the hysteretic loop is greater for the hill material.
- The materials with the broad grain-size distribution are stronger and stiffer than those with the narrow grain-size distribution. The increase of strength and stiffness is more pronounced for the hill material.

If moisture is added to the hill material, then it will behave like an unsaturated granular material. The hill material with the broad grain-size distribution is made wet before being subjected to the triaxial test described above. The wet material has a 20 kPa suction added between all grains that are within 3 mm of one another at the end of material genesis.<sup>18</sup> The stress-strain responses of the dry and wet hill materials are compared in Figure 22. The stress-strain responses are similar, and the resilient modulus is increased for the wet material.

{DP: Generate new plots for Figs. 20-22 with y-axes labelled “-Deviator Stress (kPa)”.}

{DP: Perform a UCS test on the wet hill material described in the preceding paragraph. It may be necessary to reduce the material pressure during the dry packing process to 20 kPa. We expect the response to be similar to that of the wetted glass beads described in Richefeu et al. (2008): (a) the axial stress versus axial strain curve is steep, and then reaches a peak and remains plastic-like; and (b) a plot of peak axial stress (UCS) versus water content gives an increase of UCS (from 0 to 300 Pa) with increasing water content (from 0 to 12 percent).}

---

<sup>18</sup> The suction is typical for aggregates with gravimetric moisture content ranging from 5 to 10 percent.

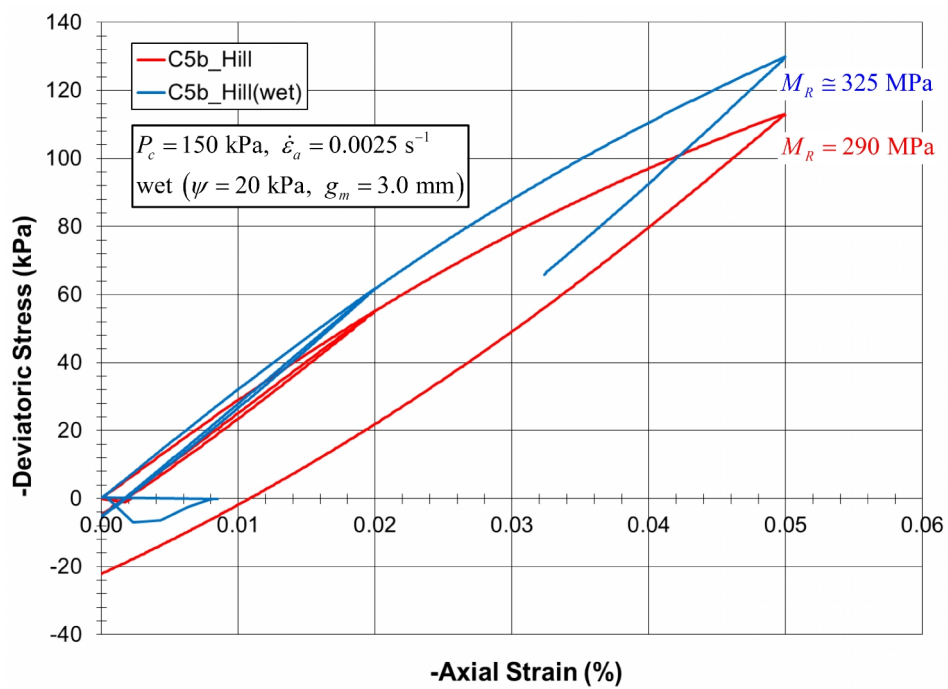


**Figure 22** Deviator stress versus axial strain for dry and wet hill materials with broad grain-size distribution tested at 150 kPa confinement.

### 3.0 REFERENCES

- Gupta, S.C., and W.E. Larson. (1979) "Estimating Soil Water Retention Characteristics from Particle Size Distribution, Organic Matter Percent, and Bulk Density," *Water Resources Research*, **15**, 1633–1635.
- Gupta, S., A. Ranaivoson, T. Edil, C. Benson, and A. Sawangsuriya. (2007) "Pavement Design Using Unsaturated Soil Technology," Minnesota Dept. of Transportation, Saint Paul, Minnesota, MnDOT 2007-11, 2007.
- Gupta, S., A. Singh, and A. Ranaivoson. (2005) "Moisture Retention Characteristics of Base and Sub-base Materials," Minnesota Dept. of Transportation, Saint Paul, Minnesota, MnDOT 2005-06, 2005.
- Itasca Consulting Group, Inc. (2016) *PFC—Particle Flow Code in 2 and 3 Dimensions*, Version 5.0, Documentation Set of version 5.00.27 [September 5, 2016]. Minneapolis: Itasca.
- Itasca Consulting Group, Inc. (2008) *PFC3D—Particle Flow Code in 3 Dimensions*, Version 4.0, User's Manual. Minneapolis: Itasca.
- Lian, G., C. Thornton and M.J. Adams. (1993) "A Theoretical Study of the Liquid Bridge Forces between Two Rigid Spherical Bodies," *J. Colloid and Interface Science*, **161**, 138–147.
- Mindlin, R.D. (1949) "Compliance of Elastic Bodies in Contact," *Journal of Applied Mechanics*, **16**(3), 259–268. Also cited as *Journal of Applied Mechanics, Transactions ASME*, **71**, A-259–268.
- Mindlin, R.D., and H. Deresiewicz. (1953) "Elastic Spheres in Contact Under Varying Oblique Forces," *Journal of Applied Mechanics*, **20**(3), 327–344.
- Muguruma, Y., T. Tanaka and Y. Tsuji. (2000) "Numerical Simulation of Particulate Flow with Liquid Bridge between Particles (Simulation of Centrifugal Tumbling Granulator)," *Powder Tech.*, **109**, 49–57.
- Potyondy, D. (2016) "Material-Modeling Support in PFC [fistPkg24]," Itasca Consulting Group, Inc., Technical Memorandum ICG7766-L (October 12, 2016), Minneapolis, Minnesota.
- Potyondy, D. O. (2015) "The Bonded-Particle Model as a Tool for Rock Mechanics Research and Application: Current Trends and Future Directions," *Geosystem Engineering*, **18**(1), 1–28.
- Potyondy, D., and S. Emam. (2009) "A Particle-Based Model for Studying Excavation Damage at Tournemire Underground Laboratory — Phase II: Hydric Damage and Tunnel Simulations," Itasca Consulting Group, Inc., Report to Institute of Radioprotection and Nuclear Safety (IRSN), Fontenay-Aux-Roses Cedex, France, ICG09-2454-13, May 2009.

Potyondy, D., and S. Emam. (2008) "A Particle-Based Model for Studying Excavation Damage at Tournemire Underground Laboratory — Phase I: Relevant Mechanisms," Itasca Consulting Group, Inc., Report to Institute of Radioprotection and Nuclear Safety (IRSN), Fontenay-Aux-Roses Cedex, France, ICG08-2454-31, October 21, 2008.

Potyondy, D., J. Siekmeier, and L. Petersen. (2016) "Aggregate-Geogrid Interaction Model Incorporating Moisture Effects," in Transportation Research Board 2016 Annual Meeting Compendium of Papers.

Richefeu, V., M.S. El Youssoufi, R. Peyroux and F. Radjai. (2008) "A Model of Capillary Cohesion for Numerical Simulations of 3D Polydisperse Granular Media," *International Journal for Numerical and Analytical Methods in Geomechanics*, **32**(11), 1365–1383.

Tan, D., K. Hill and L. Khazanovich. (2014a) "Quantifying Moisture Effects in DCP and LWD Tests Using Unsaturated Mechanics," Dept. of Civil Engr., University of Minnesota, Final Report to Minnesota Dept. of Transportation, Saint Paul, Minnesota, MN/RC 2014-13, February 2014.

Tan, D.S., L. Khazanovich, J. Siekmeier and K.M. Hill. (2014b) "Discrete Element Modeling of Effect of Moisture and Fine Particles in Lightweight Deflectometer Test," *Transportation Research Record: Journal of the Transportation Research Board*, No. 2433, 58–67, 2014, DOI: 10.3141/2433-07. Washington, D.C.: Transportation Research Board of the National Academies.

Timoshenko, S.P., and J.N. Goodier. (1970) *Theory of Elasticity*, Third Edition, New York: McGraw-Hill Book Company, Inc.

Tsuji, Y., T. Tanaka and T. Ishida. (1992) "Lagrangian Numerical Simulation of Plug Flow of Cohesionless Particles in a Horizontal Pipe," *Powder Tech.*, **71**(3), 239–250.

## APPENDIX A: INCREMENTAL UPDATE OF SHEAR FORCE

The present implementation of the Hill model differs from Tan et al. (2014b) by providing an incremental (as opposed to an absolute) update of the shear force, which is believed to be more appropriate for static grain assemblies. The justification for this modification is presented here.

The present implementation performs an incremental update of the shear force (of the form  $\mathbf{F}_s^* = (\mathbf{F}_s)_0 - \tilde{k}_s \delta_o^{1/2} \Delta \delta_s + \mathbf{F}_s^d$  where  $(\mathbf{F}_s)_0$  is the shear force at the beginning of the time step) as opposed to an absolute update (of the form  $\mathbf{F}_s^* = -\tilde{k}_s \delta_o^{1/2} \delta_s^e + \mathbf{F}_s^d$  where  $\delta_s^e$  is the effective shear overlap). The absolute update does not pass the following physical thought experiment (see Figure 23). Constrain the motion of the two particles such that all motion is imposed. Apply a relative normal displacement  $(\delta_o)_A$  and keep this value constant while applying a relative shear displacement of  $(\delta_s)_A$  to obtain a shear force  $(F_s)_A$ . Double the relative normal displacement (such that  $(\delta_o)_B = 2(\delta_o)_A$ ). What should happen to the shear force? The shear force should not change. Using an absolute update will increase the shear force, whereas using an incremental update will not change the shear force. As the shear force responds to relative shear motion, the current effective shear stiffness should be employed to obtain incremental updates to the shear force.

If shear-force update is

$$\text{absolute, then } (F_s)_B > (F_s)_A$$

$$\text{incremental, then } (F_s)_B = (F_s)_A.$$

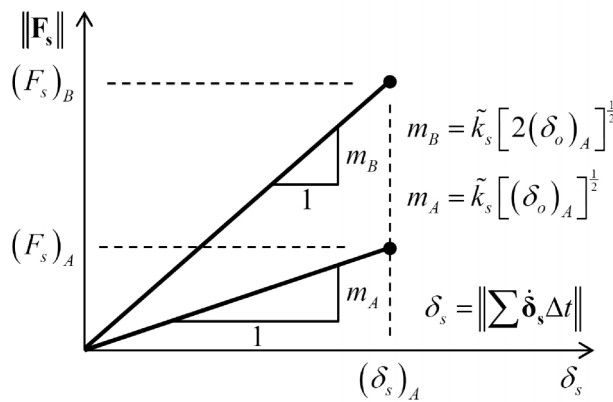


**Figure 23** Physical behavior during thought experiment in which the overlap is doubled. The shear force should not change. An absolute update of the shear force will increase the shear force, whereas an incremental update of the shear force will not change the shear force.